University of Kentucky

UKnowledge

2012

MAGNETIC FIELDS AND OTHER PHYSICAL CONDITIONS IN THE INTERSTELLAR MEDIUM

Furea Kiuchi
University of Kentucky, kiuchi@pa.uky.edu

Right click to open a feedback form in a new tab to let us know how this document benefits you.

STUDENT AGREEMENT:

I represent that my thesis or dissertation and abstract are my original work. Proper attribution has been given to all outside sources. I understand that I am solely responsible for obtaining any needed copyright permissions. I have obtained and attached hereto needed written permission statements(s) from the owner(s) of each third-party copyrighted matter to be included in my work, allowing electronic distribution (if such use is not permitted by the fair use doctrine).

I hereby grant to The University of Kentucky and its agents the non-exclusive license to archive and make accessible my work in whole or in part in all forms of media, now or hereafter known. I agree that the document mentioned above may be made available immediately for worldwide access unless a preapproved embargo applies.

I retain all other ownership rights to the copyright of my work. I also retain the right to use in future works (such as articles or books) all or part of my work. I understand that I am free to register the copyright to my work.

REVIEW, APPROVAL AND ACCEPTANCE

The document mentioned above has been reviewed and accepted by the student's advisor, on behalf of the advisory committee, and by the Director of Graduate Studies (DGS), on behalf of the program; we verify that this is the final, approved version of the student's dissertation including all changes required by the advisory committee. The undersigned agree to abide by the statements above.

<div align="right">

Furea Kiuchi, Student

Dr. Thomas Troland, Major Professor

Dr. Tim Gorringe, Director of Graduate Studies

</div>

MAGNETIC FIELDS AND OTHER PHYSICAL CONDITIONS IN THE
INTERSTELLAR MEDIUM

DISSERTATION

A dissertation submitted in partial
fulfillment of the requirements for
the degree of Doctor of Philosophy
in the College of Arts and Sciences
at the University of Kentucky

By
Furea Kiuchi
Lexington, Kentucky

Director: Thomas Troland, Professor of Physics and Astronomy
Lexington, Kentucky 2012

ABSTRACT OF DISSERTATION

MAGNETIC FIELDS AND OTHER PHYSICAL CONDITIONS IN THE
INTERSTELLAR MEDIUM

This document consists of two very different projects but the common thread is in the interest of magnetic fields. It describes the effect of magnetic fields in two Interstellar Medium regions in the Galaxy. Electromagnetic force is one of the four fundamental forces in physics. It is not known where magnetic field has initially risen in the Universe, but what is certain is that it has significant effect in the dynamics of star formation and galaxy formation. The studies aim to better understand the effects of field in an active star forming region and in the halo of the Galaxy. We observed the HI 21 cm spectral line via the Zeeman effect in attempt to detect line-of-sight magnetic field strengths in both of the projects. For the star forming region project in Chapter 2, towards the Eagle Nebula, an upper limit of the field strength was determined. From the observational results, physical conditions of the region were modeled. For the second project in Chapter 3, we attempted to detect magnetic fields via Zeeman effect towards non galactic disk objects. All of the observed positions have radial velocities that cannot be explained by the simple galactic rotation. Hence, they are considered to be non galactic disk sources and often grouped as High Velocity Clouds. With a unique observational technique and analysis, we derived the best fit line-of-sight magnetic fields. A particular interest to us is the Smith Cloud. From the detection of magnetic field, we attempted to estimate the density of the ambient medium in the halo, which will be useful for studying the galaxy formation

KEYWORDS: ISM, Magnetic Fields, Zeeman Effect, Polarizations

Author: Furea Kiuchi

Date: December 6, 2012

MAGNETIC FIELDS AND OTHER PHYSICAL CONDITIONS IN THE
INTERSTELLAR MEDIUM

By

Furea Kiuchi

Thomas Troland
Director of Dissertation

Tim Gorringe
Director of Graduate Studies

December 6, 2012
Date

To my family, especially my parents who have let me avoid the reality until now...

ACKNOWLEDGMENTS

TABLE OF CONTENTS

LIST OF TABLES

LIST OF FIGURES

Chapter 1 Introduction

1.1 Interstellar Material

When humans have looked at the sky in the past, they saw only planets, stars, and galaxies, and vacuum space in between. Today, we know that at least in the Milky Way 15 % of visible mass is in the form of interstellar medium (ISM), which fills up space between stars inside galaxies. What fills up space in between galaxies are called intergalactic material (IGM). ISM is the source of stellar births, thus studying the dynamics of ISM is a key to understanding star formation as well as galaxy formation. ISM mostly exists in the diffuse form whose average density in the Galaxy is about 1 hydrogen atom per cubic centimeter. The diffuse ISM is thought to be not bounded by its local gravitational force. However through its internal motions and collisions of particles overtime the gas goes through gravitational collapse, becomes dense and eventually forms stars. How diffuse ISM *exactly* form stars still remain quite uncertain and the High Velocity Clouds (HVCs) project in Chapter 3 may also have relevance to galaxy formation if the clouds are pristine material from the IGM. In order to understand the dynamics of star formation and galaxy formation, one type of the fundamental forces that deserves attention is the electromagnetic force. Hence, the goal of this thesis is to investigate the role of magnetic fields in the process of star formation and also galaxy formation from the observational point of view.

ISM is made of 99 % gas and 1 % dust by mass. Astronomers often divide the ISM into three forms of hydrogen states, molecular state (H_2), neutral atomic state (H^0), and ionized state (H^+). Those states go from the coldest to hottest respectively. Hydrogen in the Galaxy is mostly in the form of molecular gas. A very simply analogy on how one state changes to another is as follows. When there is diffuse molecular gas, through radiation such as cosmic rays and stellar radiation from a nearby star, molecular hydrogen gets dissociated and atomic hydrogen is formed. The last state is formed when there is sufficient energy, at least 13.6 eV to be more precise, to ionize atomic hydrogen. Cosmic rays are not energetic enough to ionize hydrogen, therefore the H^+ region only exists nearby massive young stars. As a result, in a typical star forming region, there is ionized gas closest to the newly born stars, atomic gas is the second closest shielding violent stellar radiation from the molecular cloud that sits behind.

So far interstellar gas was mentioned and one may wonder the significance of dust component especially because it only makes up 1 % of the ISM mass. However, it has come to light that dust plays a very important role not only in star formation but also planetary system formation and even galaxy formation. The dust grains are composed of elements such as carbon (C), silicon (Si), magnesium (Mg), aluminum (Al), sulphur (S), calcium (Ca), iron (Fe) etc, in the solid phase, and they range in size from small aggregates of atoms up to particles in order of 1 μm in size. The details of dust formation as well as destruction are still under investigations and this topic alone can be someone's thesis, however, it is generally created in the outskirts

of red giant stars where the temperature is much cooler than its core. Even though we cannot directly determine the chemical composition of dust grains, we can infer it from depletion of chemical elements from the gas-phase ISM. Cosmic abundances can be estimated from the study of sunlight. The Sun, a typical star in the Galaxy, is hot enough to have all of the elements in the gas phase. If the gas phase ratio is much less in the ISM than it is in the Sun, it is acceptable to calculate how much of elements has been depleted out of the gas phase onto grains. The dust is also important to forming H_2, and plays as an important coolant mechanism as it absorbs ultraviolet (UV) light and emits in far-infrared (far-IR) range in the cold ISM.

1.2 Magnetic Fields

It is inevitable that magnetic fields exist in the Galaxy. They contribute to the total pressure of the galaxy, sometime work against gravity in order to sustain ISM from collapsing, and also are the key to remove angular momentum in the protostellar cloud. Even though nobody knows exactly how the magnetic fields are initially introduced in the galaxy, the well-known fact is that once they are created, they remain for a very long time. The magnitude of strengths varies depending on which region in the sky one observes. The cold neutral medium (CNM) is diffuse non-self-gravitating atomic gas. The Millennium Survey of magnetic fields in the CNM study, which was conducted by Carl Heiles and Tom Troland, shows that polarized radiation in and has revealed that the mean magnetic field strength is about 6 μG (Heiles and Troland, 2005), where the magnetic field on Earth's surface on average is about 1 G for comparison.

The influence the magnetic field has upon the dynamics of ISM is considerably important. Charged particles, ions, are directly coupled to the magnetic field due to Lorentz Force. Even though the neutral particles are unaffected by the Lorentz Force, they are indirectly coupled to the field through collisions with the ions. As a result, if formation of a denser core inside a diffuse cloud occurs, the field lines get pulled closer to each other, increasing the local magnetic density. If the core changes its position, the field moves along with the core as well. This concept is called "flux freezing", where the field is coupled to the gas as a whole. One may think that the order of 6 μG field strengths in CNM is too small to be considered significant. But because of the flux freezing, the field strength inside a denser part of the cloud can be much stronger than 6 μG.

The balance of all of the energies determines the cloud's fate. That includes gravitational energy, external pressure, internal kinetic energy, and magnetic energy.

$$U_{tot} = U_{grav} + U_{ext\ pressure} + U_{kinetic} + U_{mag} \tag{1.1}$$

In case of a spherical cloud, the Equation 1.1 becomes as follows.

$$
\begin{aligned}
U_{tot} &= 5.13 \times 10^{40} a \frac{M_{solar}^2}{R_{pc}} + 1.56 \times 10^{42} \Delta V_{km/s}^2 n_{p,0} R_{pc}^3 \\
&+ 5.38 \times 10^{42} M_{solar} \Delta V_{km/s}^2 + 9.80 \times 10^{42} b B_{\mu G} R_{pc}^3
\end{aligned}
\tag{1.2}
$$

This gives the total energy in the units of *ergs*. a is a factor for mass distribution inside the cloud; $a = 1$ for a uniform distribution and $a > 1$ for centrally condensed sphere. M_{solar} is the mass of the cloud in solar units, R_{pc} is the radius of the cloud in parsec, $\Delta V_{km/s}$ is the spectral line width in km/s, $n_{p,0}$ is the proton volume density, b factor takes care of the distribution of magnetic flux ($b \approx 0.3$ for simple field geometries), and $B_{\mu G}$ is the total magnetic field measured in μG. The energies that confine the cloud are gravitational and external pressure. The energies that are associated with support of the cloud are internal and magnetic. The virial theorem expresses the relationship between the time-average of the total kinetic energy and the total potential energy. However, changes in the ISM arise slowly, usually in millions of years, that the time averages can be removed from all of the energies. Therefore, if the cloud is stable by the virial theorem then

$$\text{U}_{\text{grav}} + \text{U}_{\text{ext pressure}} = 2\text{U}_{\text{kinetic}} + \text{U}_{\text{mag}} \qquad (1.3)$$

In either case of the self-gravitating clouds or non-self-gravitating clouds, the magnetic pressure is energetically important especially along with the concept of flux freezing. For self-gravitating clouds, magnetic pressure is thought to be significant. This case is seen in molecular cores and also in star forming regions, such as our project on M16 in Chapter 2. Therefore, the influence of magnetic field component is investigated. The HVC project in Chapter 3 is the latter case of the non-self-gravitating clouds. HVCs are diffuse ISM, where the magnitude of the magnetic field effect is known very little, therefore this project attempts to examine this issue.

1.3   Polarization

Electromagnetic waves are transverse waves so they are perpendicular to the propagation of the waves. As the wave propagates, the electric field vector can be fixed to an angle, which is the case of linear polarization, or can rotate, which creates a circular polarization. It was first observed by Hiltner (1949) and Hall and Mikesell (1949) that the light which either passes through ISM or that is emitted by ISM gets polarized due to the content of dust. The mechanism for polarization is as follows. Dust grains are mostly irregular shaped, therefore have a preferred spin axis which creates the greatest moment of inertia. Let me introduce magnetic field that passes through ISM which contains spinning grains in random direction. If the spin is in the plane of the magnetic field, B, the grain feels friction from the magnetic force, which causes energy loss, and slows down. If the spin is perpendicular to the force, the grain feels no effect from the field and keeps spinning. In other words, if the spin axis of the grain is perpendicular to the magnetic field vector, the grain feels the change in the magnetic field with time which causes the dissipation, whereas if the spin of the grain axis is parallel to the magnetic field vector, there is no change in magnetic field hence no dissipation. Eventually the latter spinning grains are the only ones that continue to spin. In such case, grains are "aligned" to the force. This means that when magnetic fields are introduced through ISM, the grains become aligned. When unpolarized starlight passes through such magnetized medium, the dust absorbs and

linearly polarizes light in the direction of B. When dust *emits* in the far-IR from those regions, the emitted light is linearly polarized perpendicular to the direction of B in the plane of sky. Then, the net linear polarization can be observed.

Circular polarization is such that the electric field vector ($\vec{E}$) rotates as it propagates whereas $\vec{E}$ has a fixed angle in the case of linear polarization, which also can be observed. One can also think of circular polarization as summation of two linearly polarized vectors that are 90° out of phase.

1.4 Zeeman Effect

The Zeeman effect, which is also implied as an observational technique explained in detail later in this Chapter, involves the study of circular polarization, revealing the strength and direction of the line-of-sight (los) component of B.
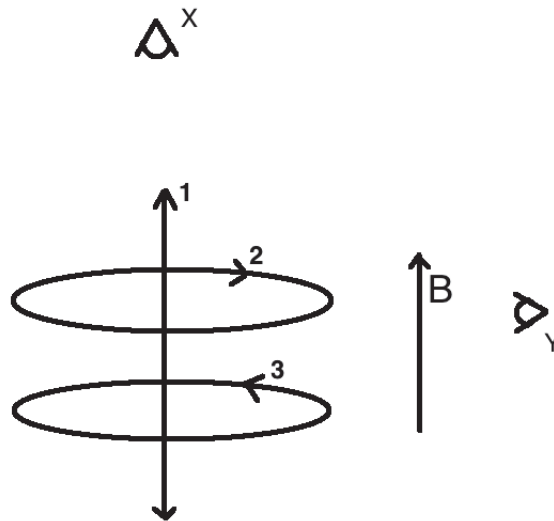
Figure 1.1: Three oscillating charged particles

Emission of radiation by Zeeman effect can be described by the viewing angle of the magnetic field from an observer. The analogy of the classical Zeeman effect perfectly explains this phenomenon. Assume that there are three oscillating charged particles as illustrated in the Figure 1.1. Particle 1 oscillates up and down in the plane of the page and also parallel to the external magnetic field, which points upward. Particle 2 and 3 oscillates circularly, in the opposite direction, in and out of the page, perpendicular to B. There are also two viewing angles, X and Y. The observer at position Y sees all three particles linearly polarized. The observer at position X does not see any radiation emitted by Particle 1, but sees radiation circularly polarized from 2 and 3, in opposite sense. From this viewing angle, Particle 2 is right-circularly polarized (RCP) and Particle 3 is left-circularly polarized (LCP).

The classical Zeeman effect in the case of the observer at position X can be derived from the equation of motion of oscillating charged particles. In the case of electrons, the motion of the two circularly moving electrons feel the centripetal force.

$$\vec{F}_{\text{circ}} = m_e \omega_0^2 \vec{r} \tag{1.4}$$

where m_e is the electron rest mass, ω_0 is the angular velocity and r is the radius of the particle from an imaginary B field line going through the center of the circle. The Lorentz law tells that a moving electrons feels force when immersed in the magnetic field.

$$\vec{F}_{\text{Lorentz}} = \frac{e}{c}(\vec{v} \times \vec{B}) \tag{1.5}$$

where e is the elementary charge, c is the speed of light, and v is the linear velocity, which is also written as $v = r\omega$ for a perfect circular motion. Thus, the total force those two particles feels is

$$m_e \omega^2 r = m_e \omega_0^2 r \pm \frac{ev\text{B}}{c} \tag{1.6}$$

where ω is the new angular velocity, which becomes

$$\omega = \omega_0 \pm \frac{e\text{B}}{2m_e c} \tag{1.7}$$

$$\Delta\omega = \pm\frac{e\text{B}}{2m_e c} \tag{1.8}$$

Converting the angular velocity into frequency, it becomes

$$\Delta\nu = \pm 1.40\frac{\text{Hz}}{\mu\text{G}} \tag{1.9}$$

The classical Zeeman effect perfectly derives the phenomenon, however it truly is a quantum mechanical effect because the Zeeman effect involves interaction between the net magnetic moment of atom and the external magnetic field. When an atom is submerged in an external magnetic field, there is a split of energy levels caused by the interaction of magnetic moment with the external field. The magnetic quantum number, m, ranges from -n to n where n is the principal quantum number. If n = 1 then there is a slight difference in energy between the (n, m) = (1, -1) state, the (1, 0) state, and (1, 1) state. This is called the Zeeman splitting.

1.5   21cm Spectral Line

Since the universe is made of 75 % hydrogen by mass, it is by far the most abundant element. Atomic hydrogen atoms are everywhere in the low-density neutral regions of ISM and they are detectable from the 21 centimeter hyperfine line. The 21 cm emission comes from the hyperfine splitting of the ground state hydrogen. When

the nuclear spin and the electron spin are parallel , the proton has the total angular momentum I $= \frac{1}{2}$ and the electron has the angular momentum J$= \frac{1}{2}$ as well. This makes the F= J + I = 1. When the electron spin flips and the proton and electron spins become antiparallel, a photon at 21.1 cm, measured at the frequency of 1420.4 MHz, is emitted, moving to a lower energy state of F = 0. This spin flip is a forbidden transition by the quantum selection rule. This means that for an isolated single ground hydrogen it takes about 10^7 years to undergo the transition naturally. However, in a typical ISM the number of hydrogen atoms is quite large and also due to frequent collisions, 21 cm emission can be observed almost in any direction in the sky.

   If there is an external B field, the Zeeman effect splits the F = 1 state in to 2F + 1 magnetic sub levels when the F=0 state is unaffected. Therefore, the F=1 state is sometimes referred to as the triplet whereas the F=0 is the singlet. The split causes a small energy difference between $m_F = 1$ and $m_F = $ -1 state, exactly by $\pm$ 1.40 Hz/μG as shown in Equation 1.9. This also means that the split difference has the magnetic field strength dependency in such that the higher the magnetic field is, the larger the split is. This is illustrated in Figure 1.2 below.
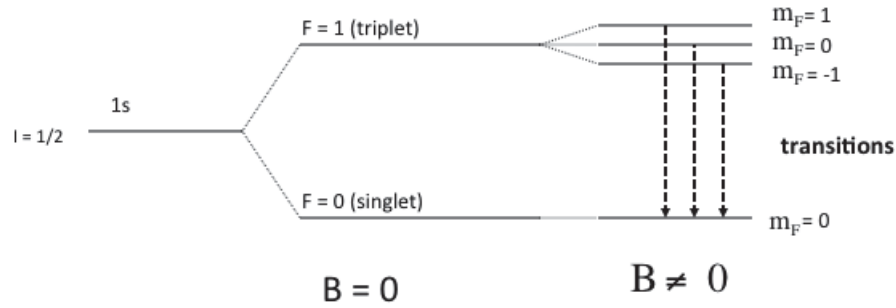
Figure 1.2: Zeeman splitting of the 21 cm line

1.6   The Zeeman Effect as the Method of Observations

When any spectral lines are observed, they all have a gaussian shape because of the internal motion of the particles and also from thermal effect. The Zeeman effect, which is a specific spectral line observation, is the only way to *directly* reveal the measurement of the magnetic field strength at astronomical distances. What makes the Zeeman observations very difficult is the fact that when two circular polarizations are observed, they are too close to be differentiable as two gaussians. Often times, the separation between them are only $\sim$ 1% their full-width at half maximum. Thus, four parameters, known as the Stokes parameters, are defined to quantify the polarized light. Mainly, two of those are of our interest for the thesis.

   In the case of interferometry, which is explained in details in Chapter 2, each antenna is sensitive to measure both senses of polarization independently, right (R)

6

and left (L). To make the use out of the interferometry, an observer must combine signals that come from a pair of the antennas. If RR represents the RCP signal and LL represents the LCP signal, then the average of those two polarizations is called Stokes I such that

$$I \equiv \frac{1}{2}(RR + LL) \tag{1.10}$$

and the half of the difference is called Stokes V,

$$V \equiv \frac{1}{2}(RR - LL) \tag{1.11}$$

A typical Stokes I profile has a gaussian shape, since it is made out of the average of two gaussians that are very close to each other. If one is subtracted from the other, its derivative is created, which is defined as Stokes V as can be seen in the above Equation 1.11. A derivative of a gaussian has an S curve 90 degrees tilted on the side. Since RR and LL have the frequency dependency, both Stokes I and V can be written as a function of ν. There is a well-known relationship between the average of the two (Stokes I) and the subtraction of the two (Stokes V) such that if magnetic field exits, the relationship between those two Stokes parameters shows a strength in magnetic field.

$$V_\nu = \frac{1}{2}(B_{los} \ b)\frac{dI}{d\nu} \tag{1.12}$$

where the constant scaling factor b is 2.8 Hz μG^{-1} for the 21 cm transition, as derived classically in Equation 1.9. Notice that the drived magnetic field in Equation 1.12 is not the total magnetic field strength, but it is the line-of-sight (los) magnetic field strength, B_{los}. If the external B field is strong enough for the separation of RCP and LCP to be seen clearly without calculating Stokes I and V, then the total magnetic field can be derived, however in the case of weak field or not being able to see the complete circular polarizations from the observer's point of view, only the line-of-sight magnetic field is derived. Thus, due to the limitation of the observer's point of view and/or weak magnetic field, a disadvantage to this observational technique is that it only reveals the line-of-sight field strength, thereby one will never know the total field strength.

The other Stokes, parameters, Q and U, give the linear polarization, while the Stokes V gives circular polarization. In the case of interferometry, if RL is created from the signal combination from a pair of the antennas, the product produces Stokes Q while the LR combination yields Stokes U. By definition in the sky coordinates respect to the horizon, Stokes Q is a linear polarization given by the difference between the vertical linear polarization and horizontal polarization. In the same respect, Stokes U is a similar combination however the two combined orthogonal polarizations are tilted by 45 degrees from Stokes Q. If the ratio of the Stokes Q and Stokes U are taken, one gets the polarization angle ϕ such that

$$\tan^{-1}\phi = \frac{Q}{U} \tag{1.13}$$

This way, one can determine the polarization angle for one that is interested in the linear polarization. However, both of the projects in this dissertation involves the studies of circular polarizations. Stokes Q and U are only briefly explained in Chapter 3, thus for the purpose of this document, Stokes Q and U are not described in details in this document.

Chapter 2 Zeeman Observations Toward M16 and Modeling Physical Conditions

2.1 Introduction

M16, more commonly known as the Eagle Nebula, is an active star forming region. A star forming region normally contains a mixture of molecular gas (H_2), atomic gas (HI) and ionized gas (HII or H^+). Those three regions correspond to the states of hydrogen since hydrogen is the most abundant element in the universe. UV stellar radiation from nearby stars dissociates molecular hydrogen to form atomic gas and also ionizes hydrogen if the photon energy is more than 13.6 eV, which is the ionization potential of H. The boundary between the neutral and ionized gas is called the ionization front, which moves into the neutral gas with time as stellar UV photons ionize more neutral gas. In this particular region in the sky, hot O and B stars in an open cluster NGC6611 are believed to be responsible for ionizing the molecular cloud (Duchéne et al., 2001).

M16 is a typical example of Photon Dominated Region (PDR) where the UV radiation from stars is strong enough to affect properties of gas such as temperature, density, and spectral emissions. The concept of PDR was first described theoretically by Tielens and Hollenbach (1985), the UV radiation governs the mechanism of gas heating and cooling. A simple model that Tielens and Hollenbach (1985) described in their paper is a semi-infinite plane-parallel slab of molecular gas being illuminated by UV radiation from a nearby star striking the PDR. In reality, the illuminated front of such gas, as well as any other places inside the gas, is not uniform in density, thus the ionization front does not move uniformly into the cloud. When the radiation encounters a dense part of the cloud known as a molecular core, the ionization front slows down, consequently, the illuminated edge has irregular shapes rather than a smooth straight-cut one. As the ionization front continues to pass around the core, the core shields the gas behind it from the stellar radiation while the surrounding cloud gets uncovered. The result is the pillars of neutral material pointing back toward the stars. One can see this effect in the most famous feature in M16, the Pillars of Creation, which became widely known after the images of Hubble Space Telescope (HST) were revealed in Hester et al. 1996.

There are various papers on M16 since it is a well studied region. Oliveira (2008) has recently reviewed the nature of the M16 region. This is a region approximately 20 pc in width, where the neutral cloud sits behind the ionized region just like Orion Nebula. Estimating a distance to an astronomical object is a hard task. The distance estimation of NGC 6611 ranges from 1.75 kpc to 3.4 kpc (Oliveira, 2008). In this document, we adopt the distance to be about 2 kpc because most of the estimated distances are around 2kpc for the cluster and as well as the nebula.

The detail mapping of the pillars has been done over many years by different people. The previous studies reveal the detection of water maser (Healy and Claussen, 2000). The most famous study in the optical wavelengths was done with HST, which

provides information about H$^+$ region (Hester et al., 1996). There are also spectral line studies in carbon monoxide (CO), which probes molecular gas, and as well as some C, which probes atomic gas (Schuller et al., 2006; White et al., 1999). Molecular clouds, sometimes referred as stellar nursery, are the perfect place to form stars via gravitational collapse since the density is the highest in ISM but the temperature is low. M16 has also been observed by an X-ray observatory, Chandra, which detects young stellar objects (Linsky et al., 2007). From the X-ray study, it has been proven observationally that new stars have been forming especially at the tip of each pillar where the ionized hydrogen sits, making M16 a very good candidate to study the dynamics of star formation.

Recently, there also have been quite a few studies of dust in this region by Spitzer Space Telescope (Flagey et al., 2011) and Herschel Space Observatory (Hill et al., 2012). Those observations show a clear morphology of where the cold and warm dust are located in this region; cold dense cloud reside in the pillars and warm dust is all over but mostly surrounds NGC6611. However, very little is known about the entire dynamics of star formation, including the effects of magnetic fields.

The goal of our study is to learn how atomic gas is distributed and also to reveal the physical properties of the famous star forming region. We started to investigate the former issue by trying to detect the line-of-sight magnetic field strengths, however, the data only allow upper limits upon B to be established. For the latter issue, our HI data along with other data in the literature allows for detailed modeling on the physical conditions.

2.2 Observations

In May and June of 2000, the HI observations were carried out at the Very Large Array (VLA) with configuration C by Tom Troland. VLA consists of 27 independent antennas, each of them has a diameter of 25 m, giving 351 independent interferometers. A huge advantage for using the interferometry is the increase of spatial resolution. Each interferometer measures a Fourier component of the two-dimensional brightness distribution of the source. Therefore, 351 different Fourier components are measured simultaneously. The field of view is determined by the beam size of an individual telescope, making it about 30' for 21 cm observations. (For details, see Appendix A in page 61). The spatial resolution depends on spacing, referred as the baseline, between each antenna, which can be changed in roughly 4 different configurations since the antennas sit on the Y shaped rail tracks. For any given configuration of the VLA, the angular resolution of an image is approximately

$$\theta \approx \frac{\lambda}{D} \tag{2.1}$$

where D is the longest baseline among the 351 baselines of the array. The purpose of the observations were to detect 21 cm HI absorption against the background radio continuum of M16, and potentially the line-of-sight magnetic field strength via Zeeman effect.

10

The radio continuum comes from free-free emissions of electrons being decelerated due to nearby protons. When the path of an electron is deflected but the electron is never captured by a proton, a photon is emitted. This is free-free emission of the electron, also known as the Bremsstrahlung radiation. This occurs at wide range of frequency since encounters between electrons and protons can occur over a continuum of distances, leading to a continuum of decelerations emitted by the electrons, hence continuum emission. The radio continuum emission comes precisely from the same emission as the optical emission. Therefore, Figure 2.4 traces the same ionized gas as Figure 2.1 and 2.3. Even though the image resolution of radio continuum may be poorer than the optical images, the radio continuum truly traces the ionized gas since it does not get absorbed by dust. The optical emission unfortunately does. This means that even though the radio continuum and optical emissions come from the same region, the images may look very different.

Both senses of the circular polarizations were observed simultaneously to detect the Zeeman effect in hope of deriving B_{los}. The total observing time was nine hours, which gave enough integration time to have high sensitivity to be able to catch a small fraction of difference between RCP and LCP. For details of the parameters, they are listed below in Table 2.1.

The VLA simultaneously obtains data at many independent but adjacent frequency channels, 256 in these data. However, the instrumental response to these various channels is not uniform, a plot of the response as a function of frequency is called the "bandpass". Therefore, one of the necessary steps in the data analysis process is to determine the bandpass function for each antenna pair and remove bandpass effects from the data. To properly calibrate bandpass corrections, the technique of alternating the sense of circular polarization passing through the telescope's IF system for every scan was used. The details of the technique are described in Brogan et al. (1999) and Brogan and Troland (2001).

Table 2.1: Parameters of VLA Observations towards M16

Parameter	Value
Frequency	1420 MHz
Observing dates	May 26, 2000 June 1
Total observing time	9 hrs
Primary beam HPBW	31.7'
Synthesized beam HPBW	19.74" × 14.26"
Phase and pointing center (J2000)	18h18m50.181 -13d48m43.90
Frequency channels per polarization	256
Velocity coverage	+89.71 km/s to -60.35 km/s
Frequency (velocity) resolution	3076Hz (0.65 km/s)
Linear scale conversion	1' = 0.58 pc [1]

[1] Assuming a distance of 2 kpc

After suitable procedures have been applied to the data from each telescope pair,a Fourier transform is applied to convert the individual Fourier components of the brightness distribution into the brightness distribution itself. The result of the transformation creates a series of images as a function of frequency. Each image is separated by a small difference in frequency ν, called a channel. When the series of images are combined together, an image data "cube" is created where the x and y components represent the coordinates in the plane-parallel sky and the z component is the frequency. When any given pixel is picked in the x-y plane, it can be plotted as a function of ν, essentially the radial velocity, and a spectrum is extracted. This is how the absorption profiles in Figure 2.6 are produced.

The Astronomical Image Processing System (AIPS) was used to reduce, calibrate, clean, image, and create the data cube for both Stokes I and Stokes V. The RCP and LCP were calibrated separately first, then combined later to calculate Stokes I (Eq. 1.10) and Stokes V (Eq. 1.11). Both Stokes I and Stokes V data cubes were CLEANed using the task called IMAGR. The calculation and derivation of optical depths was also carried out using AIPS.

2.3   Observational Results
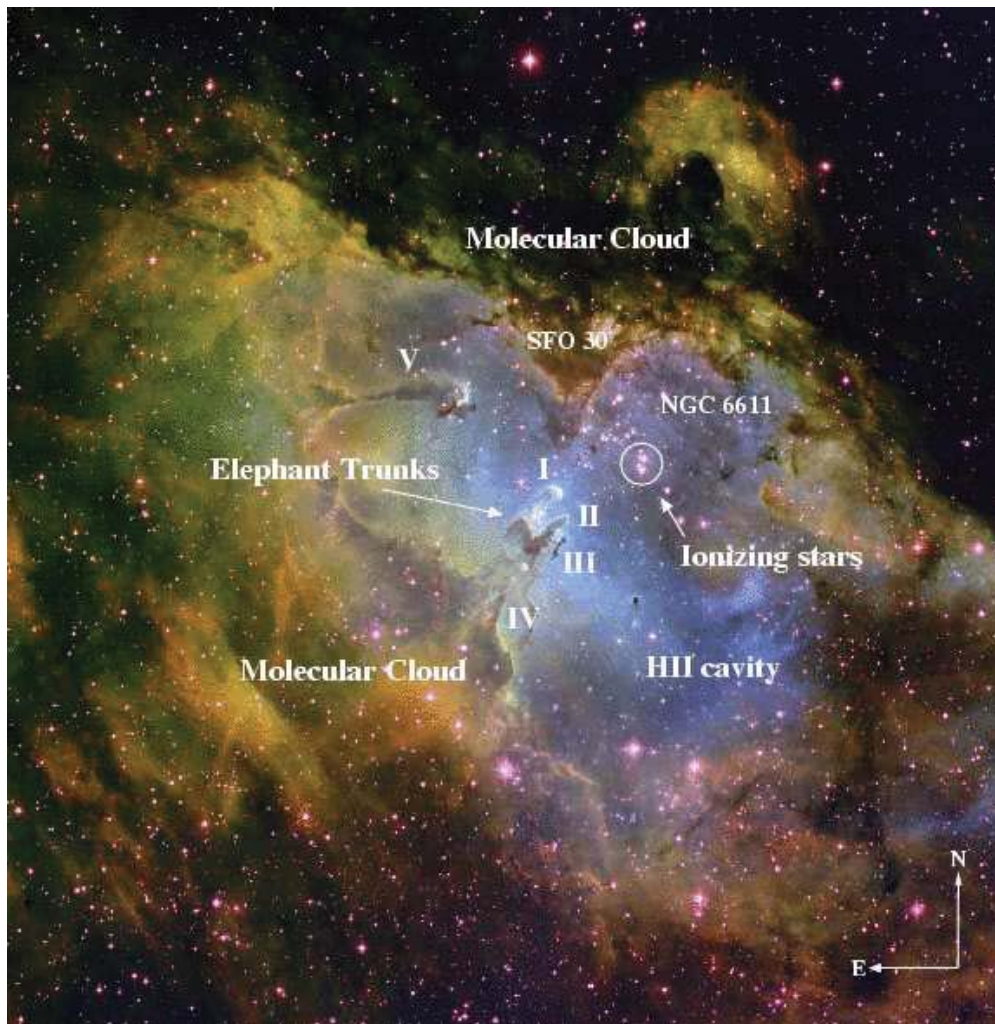
Figure 2.1: From Oliveira (2008)

Figure 2.1 is from Oliveira (2008) of optical image. The field of view is approximately 40' × 40' and this image gives convenient names to some of the features in the nebula. The Pillars of Creation, also called Elephant Trunks, is in the center of the image with the given roman numerals. The pillars Π_1, Π_2, and Π_3 are called I, II, and III. The bottom part of the pillars is given the roman numeral IV. Molecular cloud appears dark in the optical image because of the dust. NGC6611 is located in the middle of the HII cavity, where the dust has been destroyed by harsh stellar radiation.

13

Figure 2.2: Spitzer Image from three bands: blue = 4.5μm, green = 8μm, red = 24μm
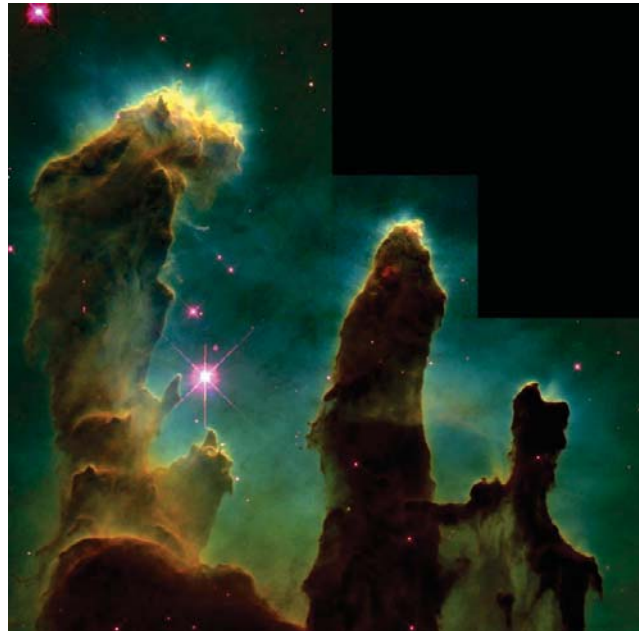
Figure 2.3: HST Image from three bands: green = Hα, red = SII, blue = OII

The above Figures 2.2 and 2.3 were obtained from the archives of each observatory. The Spitzer image shows an overall image of M16 where the HST image shows the tips of the "Pillars of Creation". Those pillars are often called, from the top left and also the largest, Π_1, Π_2 and Π_3. While the Spitzer bands trace dust in the region,

HST shows the region of ionized gas.

If a few O and/or B stars are responsible for ionizing the region, as is normally the case for a general active star forming region, it is inevitable that such stars exist in the direction all the pillars are pointing to, for the reasons mentioned in Chapter 1, and also indicated in Figure 2.1. The existence of the warm gas shown by the Spitzer 24 μm emission in the same direction also proves the presence and direction of such stars.

2.3.1 HI Continuum
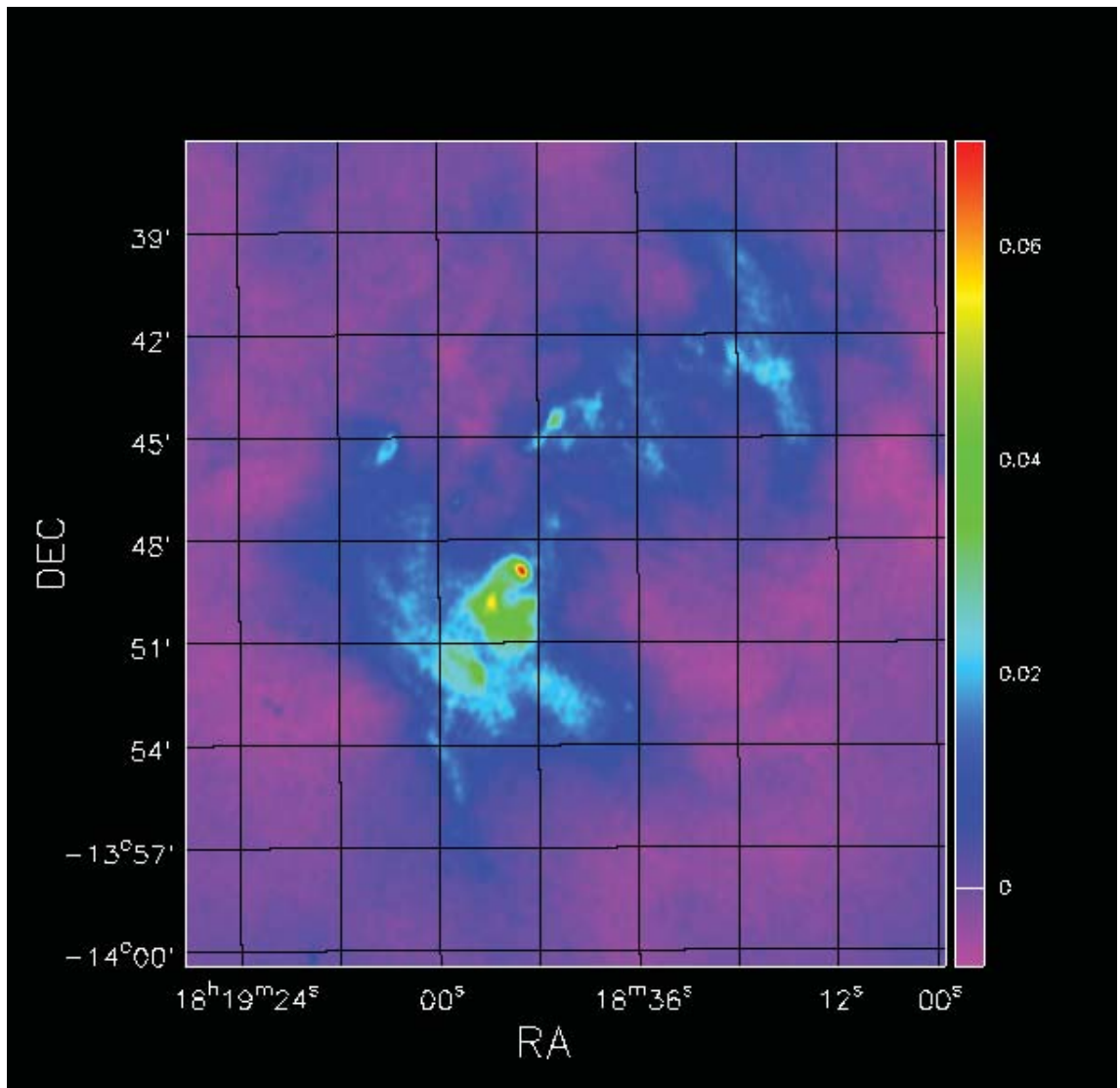
Figure 2.4: H I Continuum

Figure 2.4 is the 21 cm continuum map of M16 with $\sim$ 20" resolution with the total flux of about 30 mJy/beam with a slightly uniform weighting upon CLEANing.

Evidently, the large-scale structure of the continuum map has similar features to the Spitzer image of Fig. 2.2; one feature is the diffused gas around and below the pillars of creation, which are called filaments in Hill et al. (2012) and also called IV in 2.1 Oliveira (2008). There are a few bright continuum peaks in the pillars of creation. One is at the tip of the biggest pillar Π_1. The second peak shows up on the bottom of Π_1 where Π_1 and Π_2 meet. Where the continuum is the brightest also matches with the brightest emission in the optical images of HST, such as the tip of Π_1, which indicates that there is little-to-no dust blocking the ionized gas in that particular region. It is also important to note that even though the continuum is not very strong at the tip of Π_2, this is where the HI absorption is one of the greatest in M16, as explained later. Thus, this particular position is what we decided to pay close attention to throughout the project. Let this position define as p_0 whose position is at RA_{J2000} = 18h18m49s DEC_{J2000} = -13d49m54s .

2.3.2   HI Absorption Lines

The HI absorption lines are strongly seen in the pillars and also IV of Figure 2.1. However, at the tip of Π_1, there is virtually no HI absorption even though CO has been observed (Schuller et al., 2006). This may be due to the fact that a layer of H^+ lies in front of the neutral region from our point of view. This seems to be in agreement with the optical images: the tip of Π_1 is much brighter in the optical range than the rest of the pillar and also Π_2. This gives insight to the dimensions of the region. It is a good assumption that the same stars are illuminating both of the pillars, yet the tip of Π_1 is much brighter than Π_2 speaks the fact that Π_1 may be further away from us than Π_2.
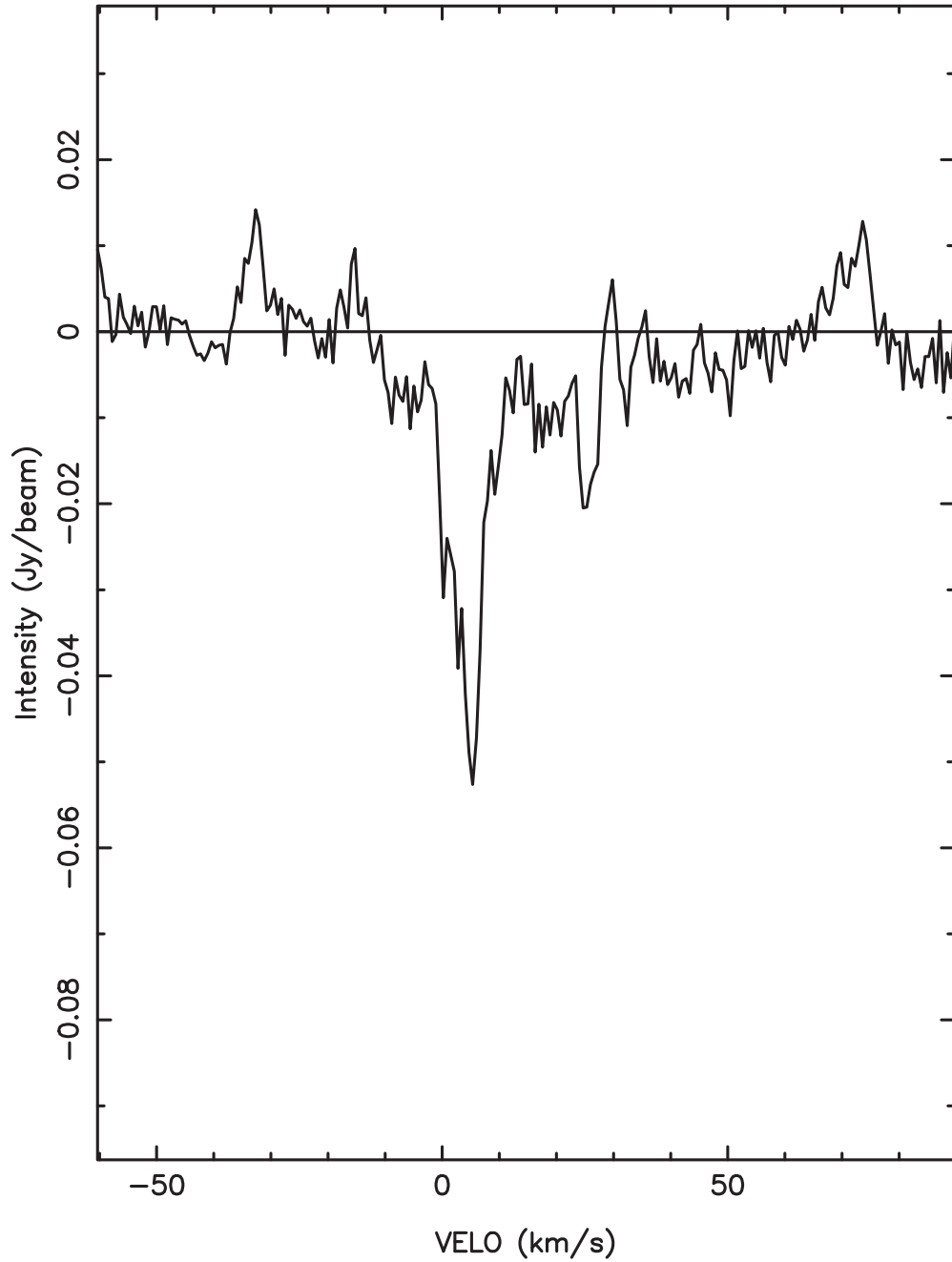
Figure 2.5: Line profile towards the tip of Π_1, RA=18h18m50s DEC=-13d48m52s. This is the same position as Fig. 2 in Schuller et al. (2006), which shows little secondary (25km/s) component

The HI absorption lines show complicated structures but consist of a few prominent velocity components towards the tips of Π_1 and Π_2. Where the absorption is the strongest has a radial velocity of ~ 5 km/s, an indication that this comes from a local cloud, not associated with M16. The other prominent velocity component

17

in the area, especially toward p_0, is at ~ 25 km/s. From the studies of other line profiles such as CO, C, and etc from Schuller et al. 2006 and White et al. 1999, it is apparent that the ~ 25 km/s component does come from M16. After examining the data cube, other than the obvious regions where there is essentially no continuum, the only place that seems to lack in the absorption is towards the tip pf Π_1.
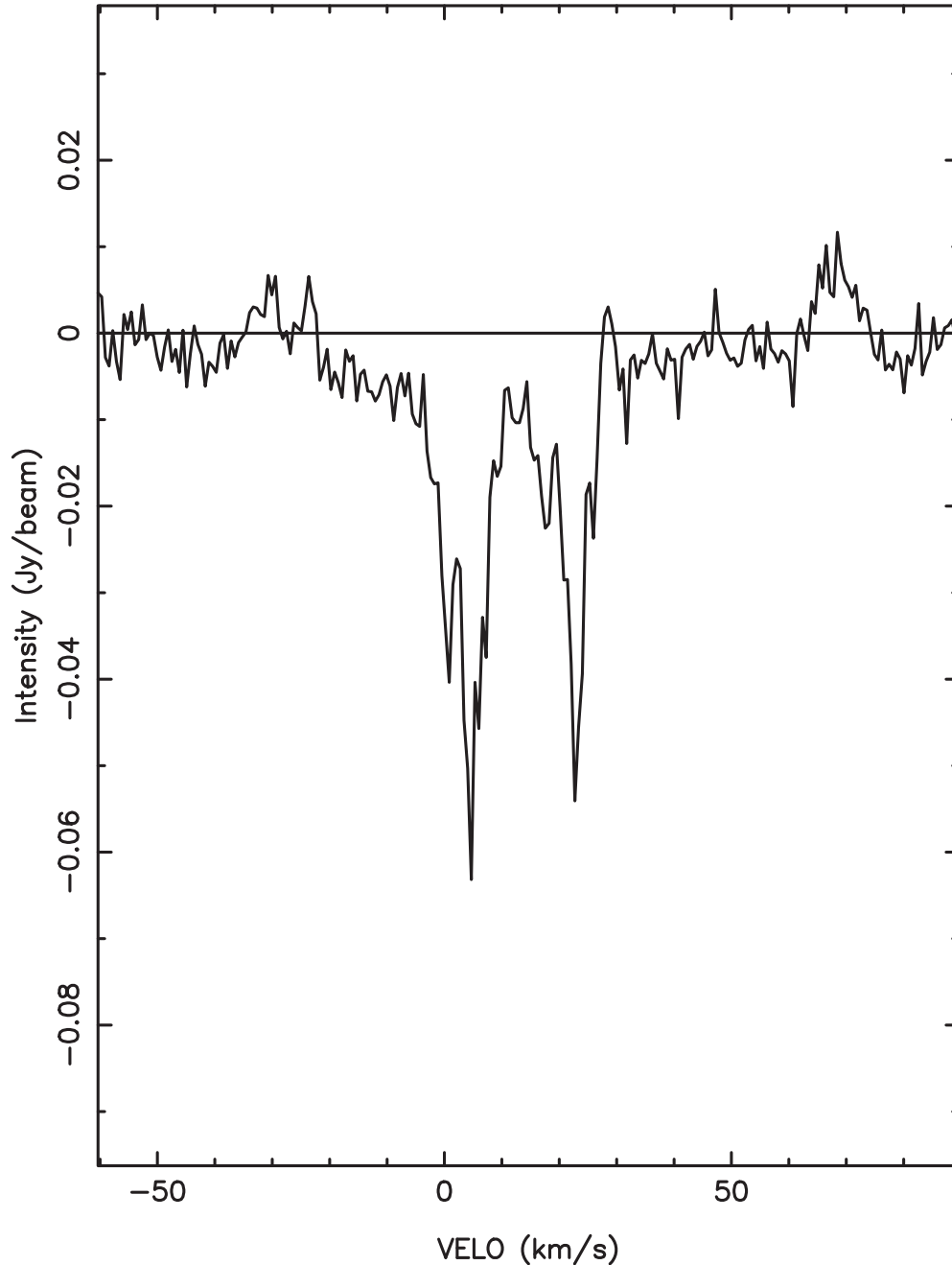
Figure 2.6: Stokes I at p_0. This is the spectral line profile of our main interest.

In Figure 2.6 above, the absorption towards M16 is much more prominent. This indicates that sufficient amount of the atomic region still exists in front of the ionized

region. Along with the CO map from Schuller et al. (2006), it is very likely that the molecular core at the position exists.

2.3.3   HI Optical Depths

From the Stokes I cube, optical depths can be calculated by the following equation.

$$\tau = -\ln \frac{I_\nu}{I_{continuum}} \tag{2.2}$$

where I_ν is the measured intensity from the Stoke I data and $I_{continuum}$ is the continuum. From the calculation of the optical depth, the column density of the atomic gas, $N(H^0)$, are calculated in such that

$$N(H^0) = 1.823 \times 10^{18} \, T_s \int \tau \mathrm{d}v \tag{2.3}$$

where T_s is the spin temperature of 21 cm. The reported column density of H_2 region at the tip of the Π_2 is $\sim 3 \times 10^{22}$ cm^{-2}, which comes from Fig. 2 of Hill et al. (2012), and it can be assumed that the most of the hydrogen is in the form of molecular towards this point. However, the image resolution is about 37", which is much lower in resolution than our HI data. While this derived column density is a good value as a reference, the column density at our resolution may be much higher, which is discussed in detail later.

Uncertainties in the calculation of the optical depth come from when $I_\nu \approx I_{continuum}$. When the intensities are similar in values, it causes the line "breakage" in the optical depth profiles, as can be seen in Figure 2.7 below towards the local cloud as an example. This breakage occurs when the optical depth is not well determined because of the uncertainty. This can happen anywhere the condition meets, hence, we note that the line profiles in the general regions of the nebula are saturated in some places.
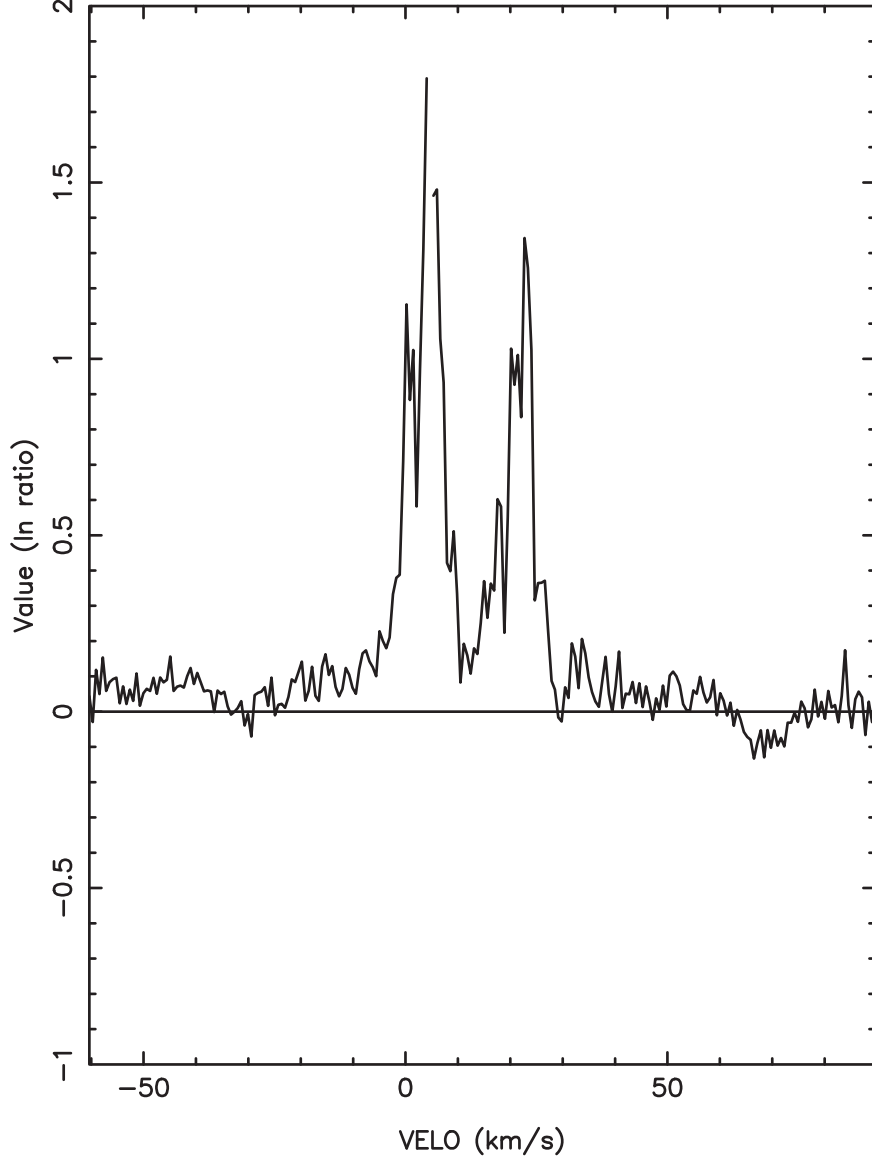
Figure 2.7: HI optical depth at p_0

Δv_{FWHM} here is roughly 3 km/s, which is in agreement with Δv_{FWHM} of CO lines from other literatures (White et al., 1999; Schuller et al., 2006), while the peak optical depth is about 1.3 . The integrated optical depth is the same as the peak optical depth multiplied by Δv_{FWHM} within a few percent. Then from these values we can rewrite the Equation 2.3 such that

$$\frac{\mathrm{N(H^0)}}{\mathrm{T_s}} = 1.823 \times 10^{18}\ \tau_{\mathrm{peak}}\ \Delta v_{\mathrm{FWHM}} \tag{2.4}$$

Towards p_0, this ratio then equals to

$$\frac{\mathrm{N(H^0)}}{\mathrm{T_s}} = 7.109 \times 10^{21} \tag{2.5}$$

20

in cgs units.

2.3.4 Magnetic Fields

The strength of magnetic field in HI can be detected from the Zeeman effect. Although it can only measure its line-of-sight strength, B_{los}, the total magnetic field, B_{tot}, is related to the line of sight by the angle θ between the total field and the observer such that,

$$B_{tot} \cos \theta = B_{los} \tag{2.6}$$

Because the width of the Zeeman split is proportional to the field strength and also typically narrow, it makes it hard to detect B_{los} with the technique. However, this is the only way to measure sensitive strengths in diffuse clouds. Generally, we consider a detection higher than 3σ to be significant. In the typical Zeeman observations, the first order analysis is to look for the "S curve" in Stokes V, which represents a scaled derivative of Stokes I, as written in Equation 1.12.

Towards M16, there was no definitive S curve pattern in Stokes V. The strength of magnetic field was then derived by a task called ZEESTAT and ZEEMAP in Multichannel Image Reconstruction Image Analysis and Display (MIRIAD). ZEEMAP calculates a derived magnetic field by fitting a derivative of Stokes I and V on a pixel-by-pixel basis using Equation 1.12. Roughly 50 pixels towards p_0 were picked and their average was taken to derive the best magnetic field strength estimation. Although we did not see the clear Zeeman effect in M16, we put the upper limit to the line-of-sight magnetic field to be 100 ± 100 μG using this technique. From this estimate, and using the 3σ condition, the maximum B is 300 μG. It is important to note that this is the first attempt in trying to find the B_{los} towards the nebula. White et al. (1999) estimated, according to their own model, the required field to be 540 μG in order to sustain the pressure equilibrium at the ionization front. However they state that their estimation of 540 μG is not appropriate for the region since the corresponding line width would be twice as much as the observed line width of $C^{18}O$. If we calculate the corresponding linewidth using our maximum B_{los} rather than their estimate, Δv is ~ 1.6 km/s which is close to their 2.2 km/s observed width. Thus, we think we have put a logical upper limit to the magnetic field strength. Later in this chapter when we examine the physical conditions of the region we put even a smaller upper limit. We will discuss in details in the next section.

2.4 CLOUDY Model

It is crucial to estimate some of the physical conditions, such as the kinetic temperature and the volume density, with some type of a model using the observational results as constraints to better understand the region. For this purpose, we use a spectral synthesis code called CLOUDY 10.00 (Ferland, 1997). CLOUDY takes in a defined radiation and the chemistry and conditions of the cloud as the inputs, and calculates emergent radiation from the cloud. The emitted spectra are then compared with the actual observational results. The input parameters get tweaked so

that the resultant emergent radiation is as close as the observed ones. Looking at the detail images of the nebula, the tip of Π_2, especially the position p_0, seems to be a much easier and practical region to model because of the simple morphology and also smooth dust emissions we see from Herschel and Spitzer images. Also Sankrit and Hester (2000) modeled the ionized region of the cloud, along a slit across Π_2, using an earlier version CLOUDY 90 to match the HST high resolution data of Hα, OIII, and SII emissivities. Since then, there have been substantial amount of published observational results that come from all ionized, atomic, and molecular regions, along with our 21cm spectral line observations to put a great deal of constraints on a model. We use the inputs of Sankrit and Hester (2000) as a template. However, since the VLA HI data resolution does not spatially match with the HST, we model the line of sight towards p_0, rather than the slit across the sky. In our model, we use a slab geometry where a distance from a star cluster to the ionization front is defined and assumes a flat cloud. The viewing angle is from the direction of the star, as shown in Figure 2.8 below.

2.4.1   Geometry of the Model

The radius, the distance between the stars and the edge of the cloud, has a large effect in the outputs of the model, yet the nature does not give us an easy problem to solve. It is fairly easy to determine a radius in the plane of sky if the plane is perpendicular and a correct distance from the observer is measured. However, there is no precise along-the-line-of-sight depth information, which is what makes the estimation of true radius impossible. As stated in the Observational Results section, it is very possible that the stars and Π_2 are not the same distance away from us. This ambiguity cannot be cleared, thus the best assumption to start out with is that the cloud and the stars reside in the plane that is perpendicular to the observer. Because of the assumption, we vary the radius of the model. We have determined that the width of Π_2 is 20" and, by adopting the distance between us and the pillar to be 2 kpc, this comes out to be around 6×10^{17} cm in the linear scale. If the line-of-sight depth of the tip of Π_2 is hemispherical, the model cloud needs to be within this thickness and particularly, we would want to create a model that would end its calculation within the half of 6×10^{17} cm since the tip is being illuminated by the nearby stars from al direction. As far as the radial distance of the edge of the cloud from the stars, called "radius", initially, the cluster of stars was put ten times the thickness of the pillar away from the illuminated front. Varying the radius changes the flux of the cloud especially the flux of Hα. The radius between a cluster of stars to the illuminated face was then varied and settled as 10^{19} cm because it best reproduced the Hα flux at the illuminated face.
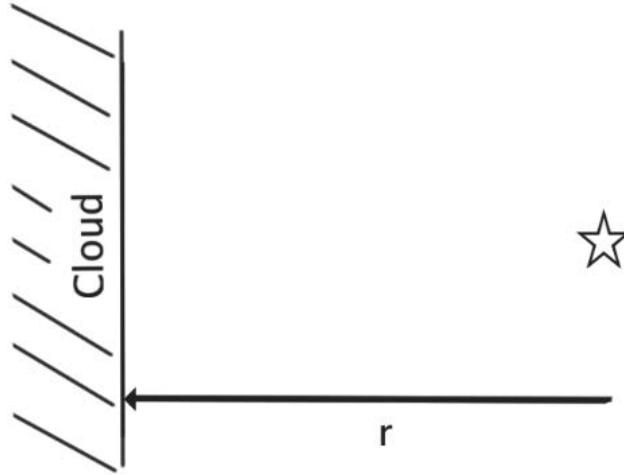
Figure 2.8: Geometry of the model

Sankrit and Hester (2000) went great length in determining chemical abundances in the region and there is no reason to assume that they are different in the ionized region and neutral region, thus, this part is kept exactly as their final values. What is different is the dimension of the model. In Sankrit and Hester (2000), they modeled along a slit in the sky, but in our model we are interested in modeling through the tip in the direction of line of sight.

All of the observed line profiles have been broadened by the Dopper effect, which is mostly due to macroscopic motions of the cloud called turbulence. Most of the line profiles have full width at half maximum (FWHM) of 3-4 km/s towards p_0. If we assume that the line broadening is mainly due to turbulence, then the observed line width at FWHM is

$$\Delta v_{\mathrm{FWHM}} = 2\sqrt{\ln 2} \ v_{\mathrm{Doppler}} \tag{2.7}$$

This equation above is given in the CLOUDY documentation (Ferland, 1978). Then the turbulence, v_{Doppler}, is set to be 1.8 km/s.

Cosmic rays are synchrotron emissions by mostly protons and electrons moving around the galactic magnetic field at relativistic speed. Such radiation can ionize atoms, thus important to neutral and molecular regions. The setback is the fact that observing cosmic rays is impossible since it is shielded by Earth's magnetic field. For the modeling purpose, we start out using the default value, which is a measured value near the Sun's vicinity, then vary to best fit the observed data.

2.4.2 Stellar Content

The amount and shape of stellar radiation hitting the nebula are what ultimately governs the PDR. The stellar cluster NGC 6611 is responsible for illuminating the

HII region of M16. The hottest star is thought to be O3-O4, which dominantly ionizes the region (Hillenbrand 1993, Hester 1996 & Evans 2005). However, when modeling the HI region is considered, what matters more is the cooler and less massive stars because the majority of their radiation contains the non-ionizing radiation. But a few hot young stars normally outshine those cooler stars, they are often unobservable, therefore we use a Salpeter initial mass function (IMF) to estimate the number of stars in the cluster, down to B5 V stars, assuming all of the hottest stars have been identified. The details are mentioned in Pellegrini et al. (2007) Section 3. For this project, the Castelli and Kurucz (2004) stellar atmosphere models were used to include the stars in our model. For simplicity, from the IMF we create a star cluster such that the log of total number of ionizing photons emitted by the stellar cluster, $Q(H)$, is 50.235 $[s^{-1}]$ and put all of them at $\log(radius) = 18.7$ cm away from the illuminated face.

In order to estimate the number of OB stars in NGC6611, the IMF with a slope of -1.35 is used to include from the brightest O stars down to B5 stars to form a star cluster that best represents NGC6611. It is essential to include B stars especially when the model needs to predict information not only an ionized region but also a neutral region. The brightest star in NGC6611 is considered to be O3.5 V, which sets the starting point of using IMF (Oliveira, 2008). We followed the argument of Pellegrini et al. (2007) to decide that the cutoff of our star cluster is B5 stars as well.

Table 2.2: Assumed Stellar Content of NGC6611

Spectral Type	T_{eff} [K]	Mass Range $[M_\odot]$	# stars	log Q(H) $[s^{-1}]$
O3 - O4	48,670	70 - 55	1	49.70
O4 - O5	46,120	55 - 45	1.12	49.57
O5 - O6	43,560	45 - 38	1.20	49.41
O6 - O7	41,010	38 - 32	1.55	49.31
O7 - O8	38,450	32 - 26	2.42	49.25
O8 - O9	35,900	26 - 22	2.50	48.95
O9 - B0	33,340	22 - 15	8.39	49.08

Spectral Type	T_{eff} [K]	Mass Range $[M_\odot]$	# stars	absolute bolometric luminosity
B0 - B1	25,527	15 - 9.5	17.72	-7.75
B1 - B2	21,979	9.5 - 7.0	19.65	-6.82
B2 - B3	18,707	7.0 - 5.5	22.38	-5.97
B3 - B5	15,417	5.5 - 4.0	43.27	-5.63

A shape of a stellar spectral energy distribution of varies depending on the stellar model, especially for the ionizing radiation. Sankrit and Hester (2000) goes great

length to compare different models, but since our focus is the neutral region we decided to pick Castelli and Kurucz (2004) ATLAS stellar model since this had the widest range and most complete number of stellar models.

2.4.3 Density Law

Examining the HST images of Pillars of Creation, it is inevitable that due to photo-evaporative flow the total hydrogen density is the lowest when closest to the stellar cluster and exponentially grows the closer it gets to the H^+/H^0 boundary. This is also shown in Sankrit & Hester 2000. There is a well-defined boundary between the ionized region and atomic region at the tip of the pillar, which suggests that the density goes up drastically there. This is due to the fact that the total pressure of the cloud is held constant and there is a drastic temperature gap between the ionized region and the atomic region. In the ionized region, the maximum density at the illuminated face is estimated to be $n(H_{tot}) = 4000$ cm^{-3} (Sankrit and Hester, 2000), and it jumps to as high as 10^5 cm^{-3} and stays fairly constant in the neutral region (White et al., 1999). Since the total pressure of the region, which includes turbulent pressure, gas pressure, and magnetic pressure, is held constant, the volume density exponentially goes up from the ionization front towards the illuminated face and flattens out once in the neutral region. Therefore, the model has a constant pressure with the starting volume density of 3100 cm^{-3}. With the initial density and the radius, the model predicts the maximum density to be 1.1×10^5 cm^{-3} as shown in the Figure 2.9. Note that the entire thickness of the cloud is 9^{17} cm, which is not shown in the Figures 2.9, 2.10, 2.12, 2.13, an 2.14.
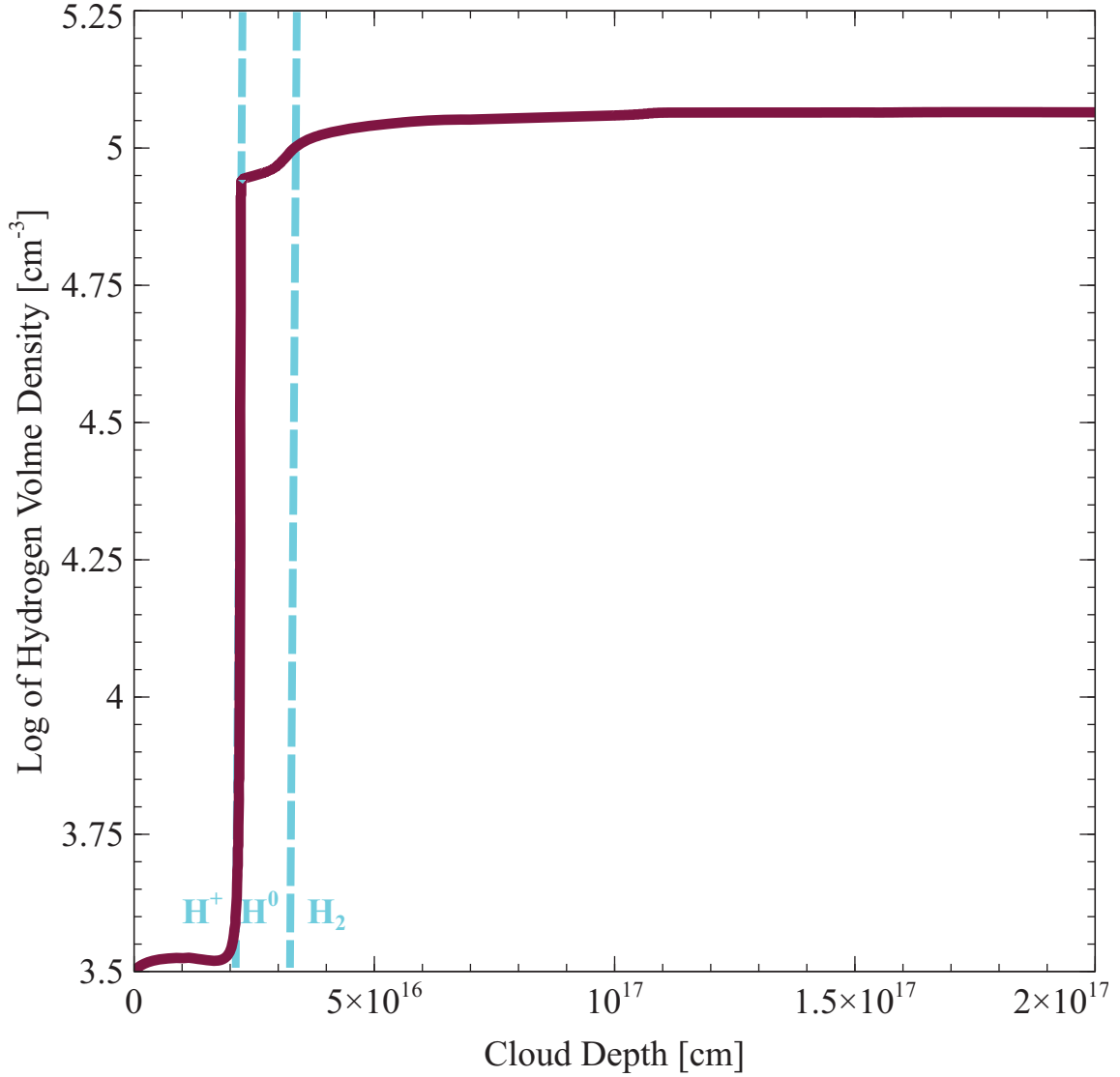
Figure 2.9: Volume density as a function of the cloud depth.

Figure 2.9 shows the volume density as a function of the cloud depth. The plot can be thought of the cloud plane slab where the stellar cluster is to the left of the plot, outside of the page, illuminating and creating the H^+ region closest to the stars. Also the three different states of hydrogen that represent the three different gas states in the ISM are represented by the dashed lines and also with the corresponding notations. This is also where the kinetic temperature of the cloud is the hottest, therefore the volume density is the lowest. At the H^+/H^0 boundary, the temperature drastically drops and to counterpart this effect, the volume density rises for the constant pressure model. There is not much of the temperature difference between the atomic region and the molecular region, thus the density flattens out.
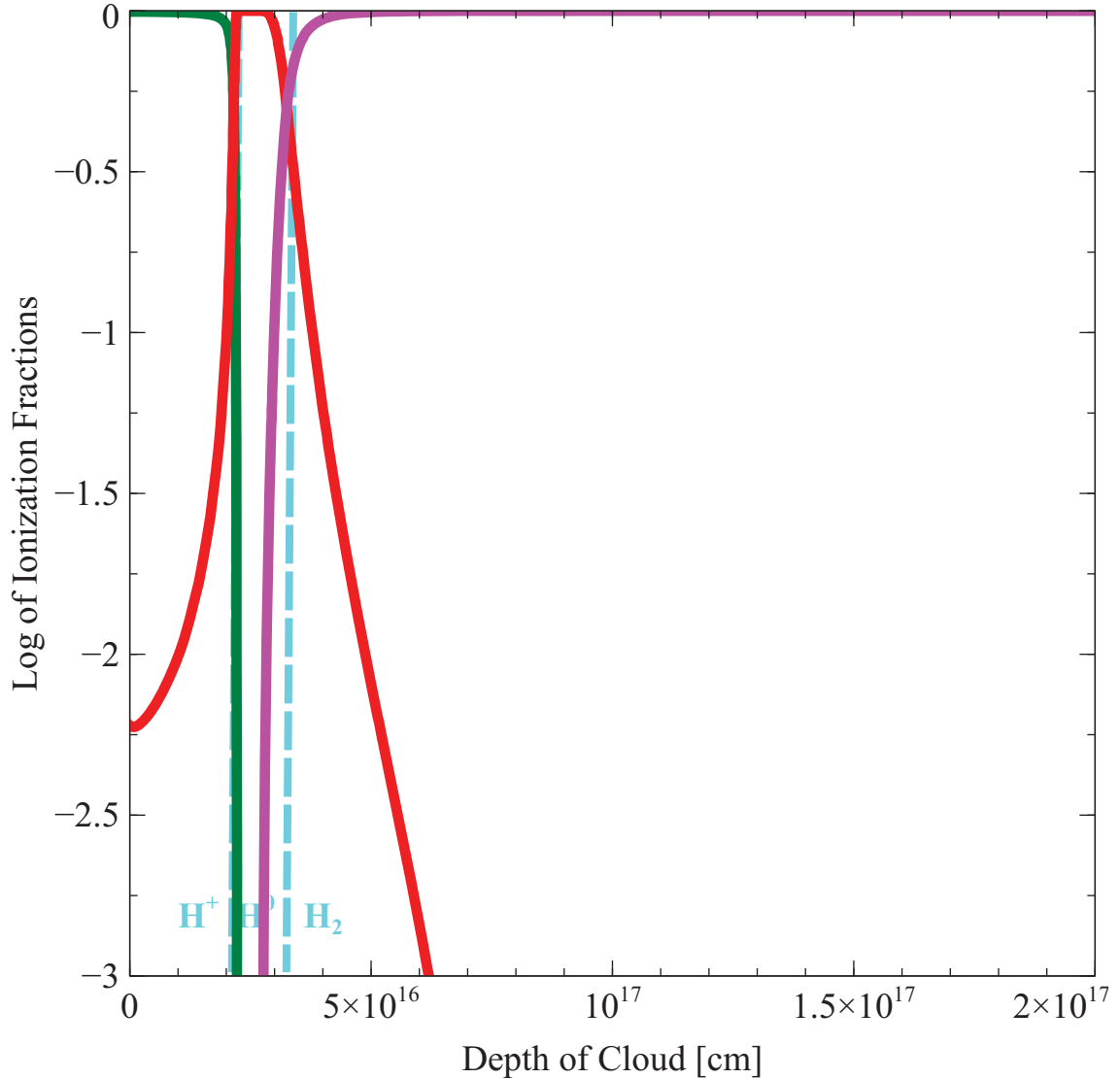
Figure 2.10: Three different hydrogen states as a function of the cloud depth.

Figure 2.10 shows the predicted three different hydrogen states in ionization fractions as a function of the cloud. The green line shows the ionization fraction of the ionized hydogen, the red line shows the ionization fraction of the atomic hydrogen, and the pink line shows the ionization fraction of the molecular hydrogen. The thickness of the atomic gas is calculated to be $\sim 1.4 \times 10^{16}$ cm, which is 2% of the entire thickness of the cloud, where the 21-cm absorption occurs.

2.4.4 Column Density

Column density is not only a stopping criteria in CLOUDY but in reality this also determines the H I absorption line as well as dust emission. Ward-Thompson et al. (2010) Equation 1 explains the relationship between dust temperature, brightness

and column density. If fluxes at different wavelengths are observed, not only the dust temperature can be estimated from fitting a modified blackbody function, but also column density can be estimated since dust emission mainly depends on the column density along the line of sight. Brightness of cloud B_ν is defined as

$$B_\nu = B_\nu(T_{\text{dust}})(1 - e^{\tau_{\text{dust},\nu}}) \qquad (2.8)$$

where $B_\nu(T_{\text{dust}})$ is the Planck function of blackbody. The equation 2.8 is sometimes called a modified blackbody function. In most cases, $\tau_{\text{dust},\nu} \ll 1$ thus,

$$B_\nu = B_\nu(T_{\text{dust}})\tau_{\text{dust},\nu} \qquad (2.9)$$

where $T_{\text{dust},\nu}$ is directly proportional to column density.

The Hershel Space Observatory is a space-based instrument designated to observe in the far-IR emissions in the 60-670 μm range. Radiation in this wavelength range comes primarily from interstellar dust particle. Hill et al. (2012) observed M16 at 70μm, 160μm, 250 μm, 350 μm, and 500 μm and also estimate the column density. At the position p_0, their estimation of the column density is about 5×10^{22} cm^{-2}. However, the 37" resolution is much lower than our H I data (20"), which may result in a lower estimation. The estimation of column density from our model input, using the volume density and the dimension of the cloud, comes out $\sim 2 \times 10^{23}$ cm^{-2}. Varying the column density does not have a great effect in the far-IR emissions. Below is flux comparison of different column densities. Note that all the results in Table 2.3 have the initial volume density of 10^5 cm^{-3} therefore the values may not be relevant to the final model, nonetheless it is clearly shown the relationship with the flux and column density.

Table 2.3: Flux of various column densities

wavelength [μm]	calculated flux [Jy/sr]		
	N(H)=10^{21}	N(H)=10^{22}	N(H)=10^{23}
2003.85	4.15E+7	4.21E+7	4.47E+7
1350.03	3.93E+7	4.16E+7	5.36E+7
852.31	3.84E+7	5.21E+7	1.17E+8
752.17	3.90E+7	5.95E+7	1.62E+8
449.45	5.85E+7	1.93E+8	7.83E+8
350.05	9.69E+7	4.21E+8	1.69E+9

Shorter-IR emissions are sensitive to the column densities but the far-IR emissions have little effect with the increasing column density. However, if the SED of any two models are plotted and compared, the one that has twice the column density calculates roughly twice as much of SED in the 100 to 800 μm range. This means that the far-IR does get emitted from deep inside of the cloud, not from a thin layer close to the illuminated front, meaning that the stellar radiation, which also carries non-hydrogen ionizing radiation, makes it deep into to the cloud.

The column density of the atomic hydrogen, N(HI), was calculated to be 10^{20} cm^{-2} for the best fit model. The column density of HI has not been observed in the region. However, there is a relationship between the optical depth and the column density as shown in Equation 2.3. The model predicts the spin temperature to be roughly 4,500 K, which makes the integrated optical depth to be 0.85. This result is very comparable to the observed peak optical depth of ~ 1 shown in Figure 2.7.

2.4.5 Dust Emission

Dust is blended in molecular clouds. Dust emission comes from both ionized region and neutral region. Therefore, as mentioned in Chapter 1, the recognition as well as understanding of dust content in ISM is a crucial component in studying a star-forming region like M16. Dust absorbs UV light, turns the energy into heat, and radiates in the IR range as a modified blackbody radiation since they are almost perfect absorbers (Equation 2.8). Young and very luminous stellar objects are born out of ISM where it is very rich in dust. The stars emit light mostly at the wavelengths that the dust grains can effectively absorb. Once the absorbed radiation is turned into internal heat, dust radiates in micron range wavelengths. Therefore, most of the dust emission in the sky comes from the star forming regions where the dust is heated by nearby stars. Also it is important to note that the IR emission from a star forming galaxy makes a significant fraction of its total radiation. Therefore, when the active star forming galaxy is observed, it is bright in the IR range.

Spitzer Space Observatory is a perfect instrument for the short to mid IR observations especially in the 3 - 20 μ m range, where most of the polycyclic aromatic hydrocarbons (PAHs) emissions occur in a broad spectrum. PAHs are comparable to the molecules in size whose grains mostly consist of carbons and their broad emissions occur at 3.3, 6.2, 7.7, 8.7, 11.3, and 12.7 μm IR bands (Salama, 2008; Tielens, 2008). Those PAH bands were once called the unidentified IR (UIR) bands but thanks to more recent studies from the space-based IR observations such as the Spitzer telescope which helped to uncover the importance of PAHs in ISM. Because the grain size is smaller than the regular ISM grains and PAHs easily get excited by ionizing radiation, in UV and optical, and emit photons in the IR ranges mentioned earlier. Therefore in a star-forming region PAH emissions are the brightest at the H$^+$/H^0 boundary. The IR bands are thought to be emitted due to the vibrational levels of PAHs to decay to the ground level. Therefore, the 8 μm emission traces the same atomic gas as our HI data. PAHs are then included in the model and the output was compared with the Spitzer data.
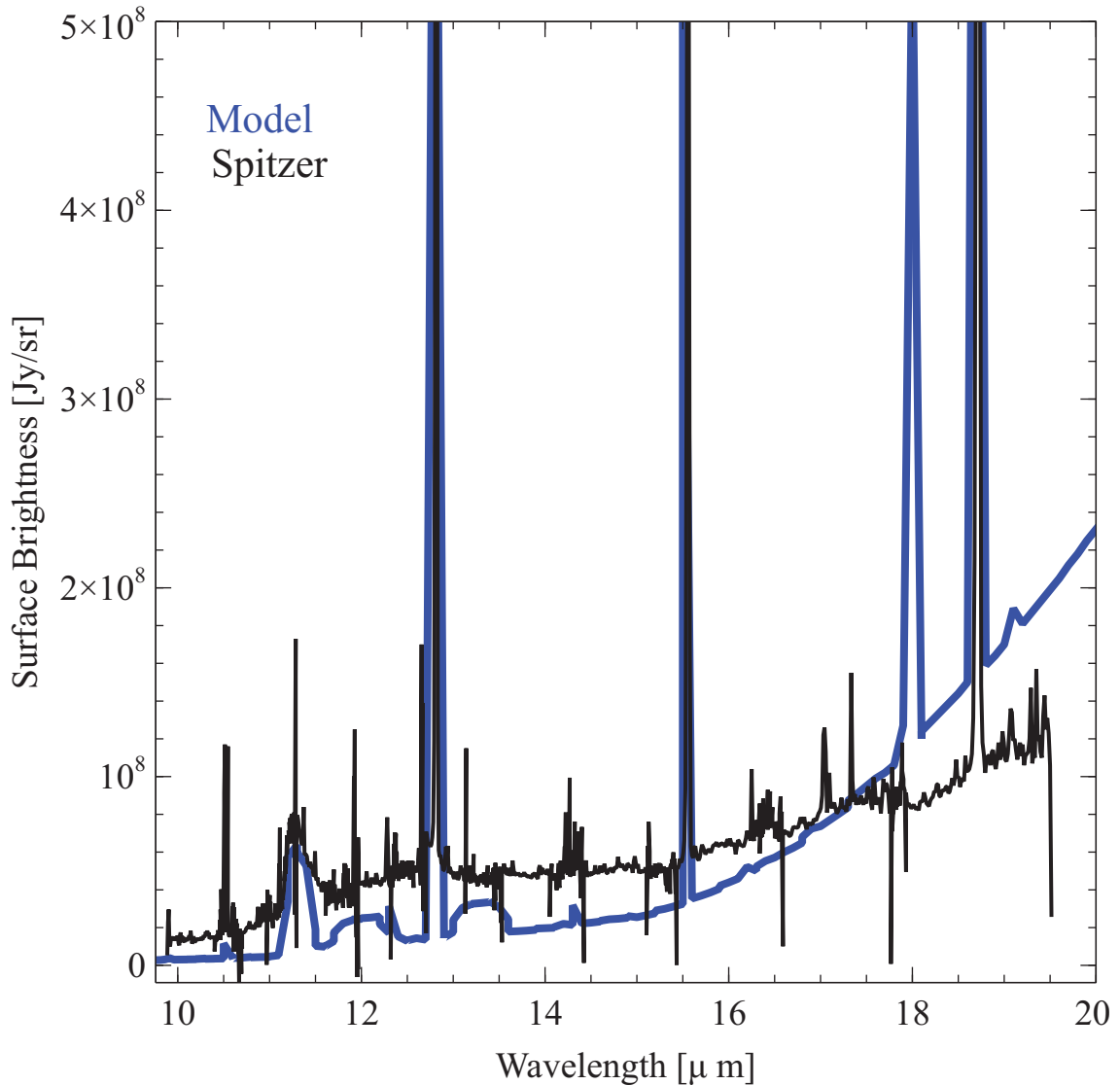
Figure 2.11: Blue: Spitzer IRS surface brightness at p_0. Black: model surface brightness with radius $= 10^{19}$ cm with ISM grains.

As expected, the emissions in those ranges change drastically with the radius. We have found that a model with the radius of 10^{19} cm produces the current best fit model, hence settling on such value. In this Figure 2.11, also for our final model, we are using the regular ISM grains, which include a size distribution and abundances that best describe the Galactic ISM content. Note that the model does produce some broader emissions around 12 μm and also around 13 μm that are not seen in the observed data. They are thought to be the PAH emissions (Tielens, 2008). Therefore, the regular ISM and the simple Orion-like PAH grains model may not explain the best dust content towards p_0. We are aware that the column density of CO in the finger is a lot less than normally expected in ISM. This is probably due to the fact that the ratio of CO to H in gas phase is a lot less, which is the result of

CO freeze-out. CO freeze-out is a phenomenon that in the cold molecular region, a fraction of CO is frozen onto grains and does not emit any radiation, which results in a less column density of CO than expected from other neutral ISM. This is a common issue in a cold dense cloud due to our poor knowledge of dust. When CO freezes out, a different dust model needs to be introduced. Preibisch et al. (1993) developed a grain model that factors in amorphous carbon grains and ice-coated silicate grains. The Preibisch-like grains produce opacity function curve described by the paper for cold ISM that is below 170 K. Therefore this may be the key to resolving some of the emissions issues. The reason for not using the Preibisch-like model is because a) the grain model is still being developed, b) even if we use the best current development version it has been determined that the optical depth of 21 cm is almost two orders of magnitude less than the observed, and c) the Preibisch-like grains are thought to only exist in the cold neutral ISM, not in the hot ionized region. This part is still under investigation and will be polished up before publication.

2.5 Summary

2.5.1 Observational Results

The H I absorption profiles show complicated structures and look different depending on a position in the region. Nonetheless, the position of our interest, named p_0, show a nice absorption indicating not only the existence of atomic gas at the tip of Π_2 but also the molecular core which shields the cloud behind it from harsh radiation coming from stellar cluster NGC6611. The 21 cm optical depth is ~ 1 at p_0, which is fairly typical in the star forming region.

   The upper limit of magnetic field is best estimated to be 300 μG, which is considerably smaller than what was estimated previously at 540 μG by White et al. (1999) with the pressure equilibrium assumption at the ionization front. Our data suggests a better constrained observational result.

2.5.2 CLOUDY Model Results

We model the tip of Π_2, p_0, along the line of sight. The final CLOUDY model contains a cluster of model stars made up of stellar radiation calculated by Castelli and Kurucz (2004). The model star cluster is positioned 10^{19} cm away from the illuminated face. The total number of ionizing photons emitted by the cluster, Q(H), is 1.58×10^{50} s^{-1}. The initial number volume density, n(H), is set at 3100 cm^{-3} with the column density of 2×10^{23} cm^{-2}. The turbulence is set to 1.8 km/s. We estimate that the starting magnetic field is $\sim 30\mu$G to make sure that not only the maximum field strength does not exceed the upper limit of $\sim 300\mu$G. Also the magnetic field is set to increase as the density to the power of 2/3 with the total cloud pressure held at constant. These input parameters combined make the line-of-sight dimension of the cloud to be 8.9×10^{17} cm.
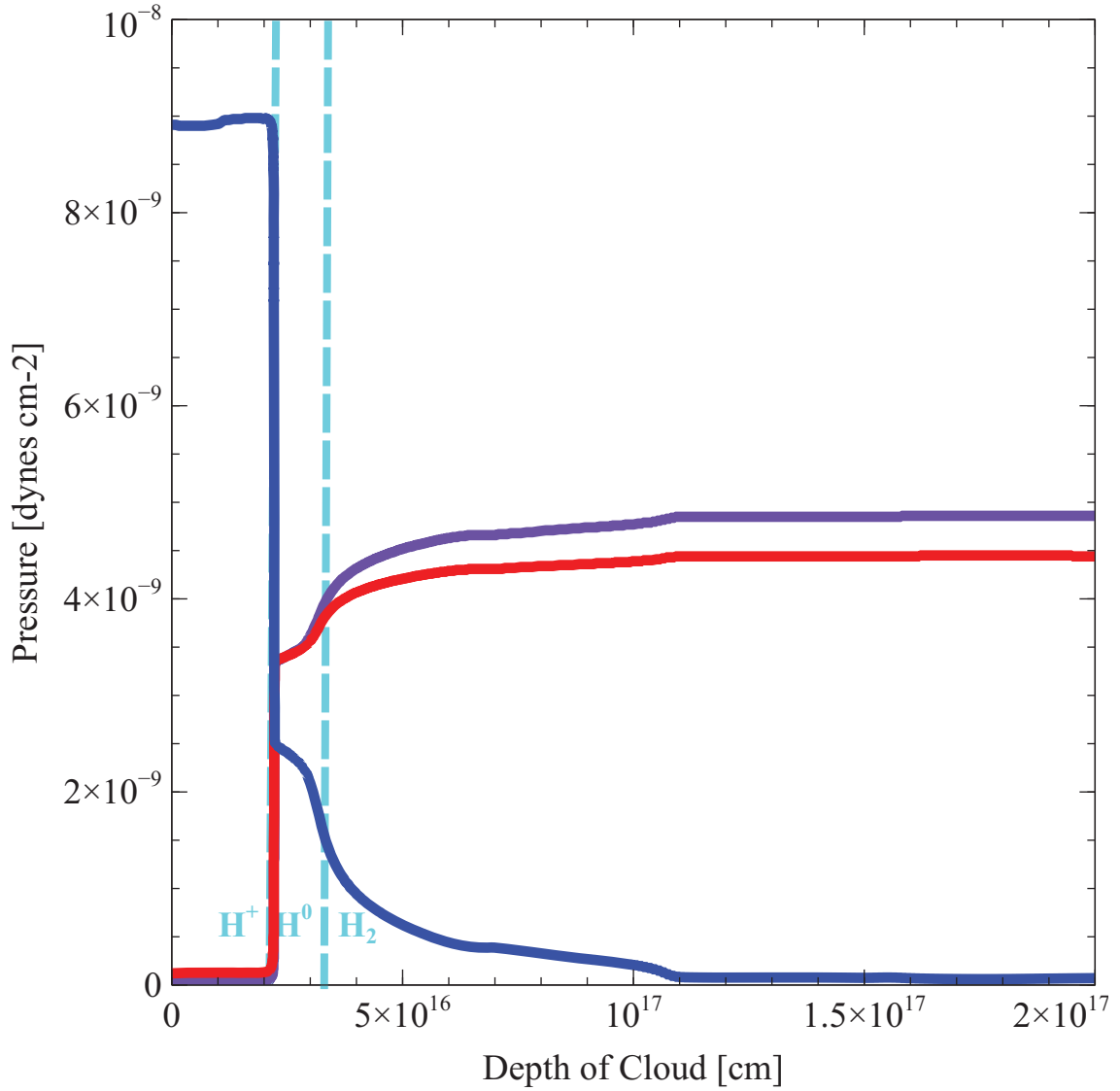
Figure 2.12: Plot of various pressures while the total pressure is held constant. The gas pressure is shown in blue, the turbulent pressure is shown in red, and the magnetic pressure is shown in purple.

The gas pressure (blue), magnetic pressure (purple), and the turbulent pressure (red) are plotted while the total pressure is held constant. The radiation pressure inside the cloud is never strong enough when compared to the other pressures thus it has been completely neglected. As can be seen in the Figure 2.12 above, in the ionized region is dominated by the gas pressure. There is a sharp drop the gas pressure at the H^+ and H^0 boundary and the other two pressures start to take over the neutral region. This explains very well of the drastic increase in the volume density in support of the molecular core at p_0. In the atomic region, the two dominant pressures make the equal contribution while the gas pressure still has some effect. In the molecular region, gas pressure gets depleted and the magnetic density and the turbulent density

are almost equivalent to each other.
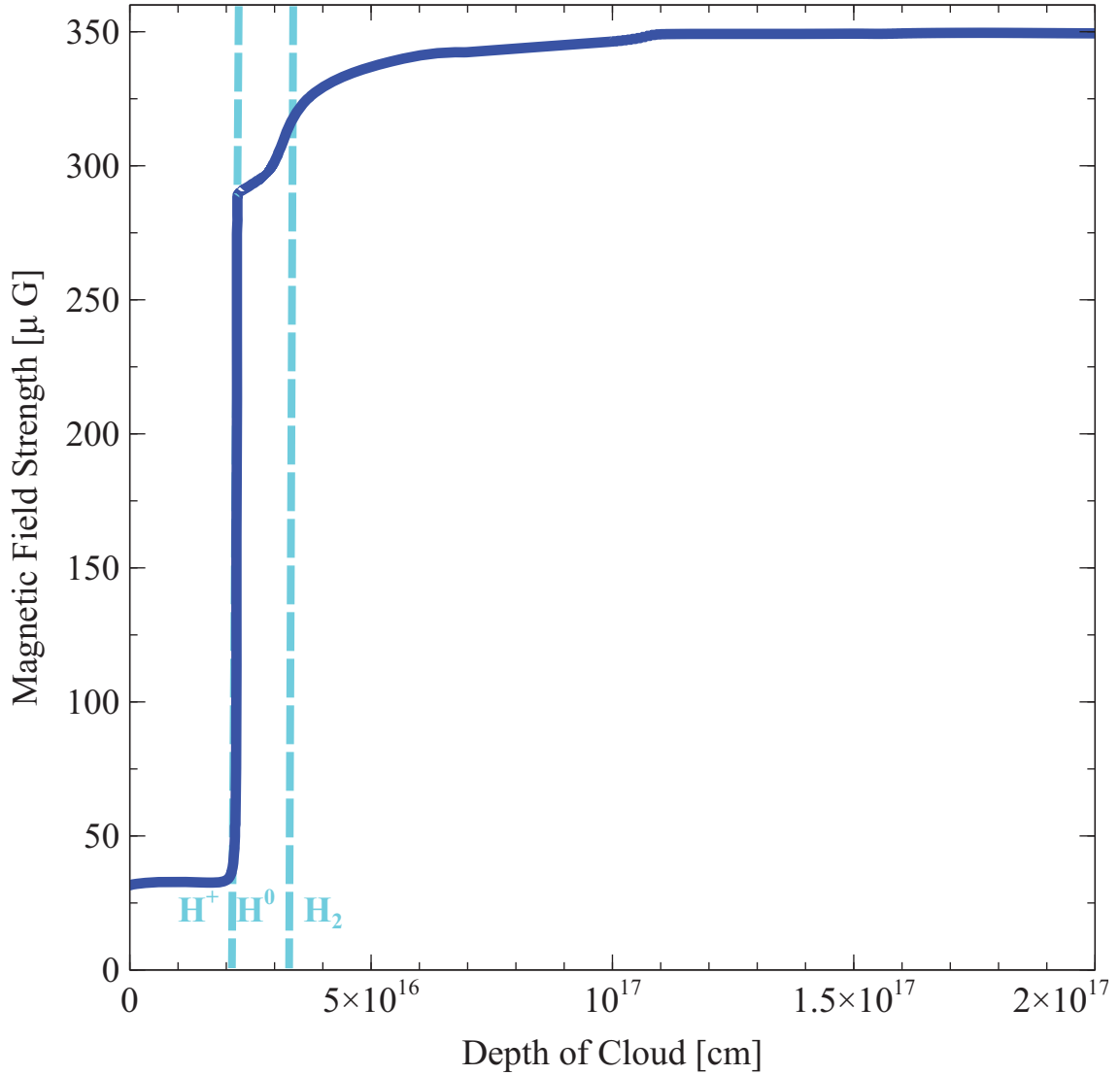
Figure 2.13: Plot of the total magnetic field at p_0 as a function of the cloud depth.

VLA H I Zeeman observations with 20" resolution have revealed the upper limit of 300 μG towards the Pillars of Creation. Our current model calculates the maximum magnetic field to be $\sim 300\mu$G, which is acceptable. Later for publication, when we refine our final model this result may vary, however we do not expect the number to be very different from our current value. Assuming constant total pressure in the model, Figure 2.13 shows how magnetic field changes as it goes deep into the cloud. Figure ?? shows the thickness of the HI region is 2 % of the total cloud thickness. This is where the magnetic field drastically increases in Figure 2.13 and increases up to $\sim 300\mu$G.
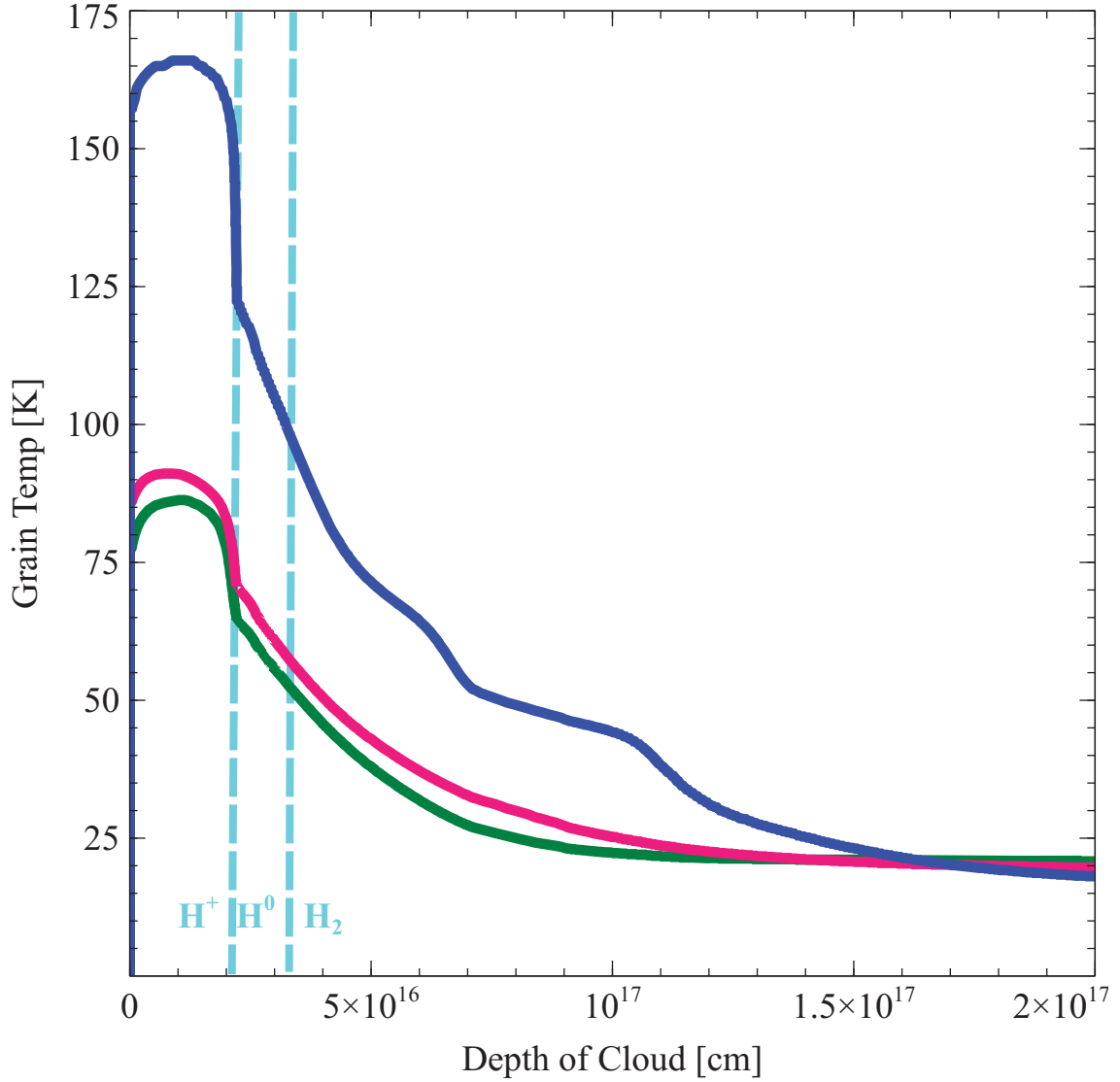
Figure 2.14: Various grain temperature. The blue line represents the temperature of PAH, the pink line represents ISM grains, and the green line represents the ISM silicate.

The Figure 2.14 above shows the temperature gradient of all the grains in the model. The PAH grains are about the size of molecules, which means they are much smaller than the regular grains. Therefore, they tend to emit in the boundary between the ionized gas and the atomic gas. If PAH gets struck by a single photon, it radiates immediately because of the size. So the addition of the energy of a single photon can significantly increase their temperature. This explains why the temperature of such grains are much higher than the others. The PAH grains are thought to freeze out on to the mantles of larger grains in the molecular gas. And the PAH grains are thought to be destroyed by the UV radiation field in H^+ regions. So the PAH grains are most likely to exist in the H^0 regions. For the other two grains, which come from

the regular Galactic ISM grain distribution, are also plotted.

Table 2.4: Comparison of Observed and Model lines M16 at p_0

Line ID	HBPW ['']	λ [μm]	$\log(SB)$[1] $\left[\frac{erg}{s\ cm^2\ sr}\right]$	$\log($CLOUDY SB$)$ $\left[\frac{erg}{s\ cm^2\ sr}\right]$	ratio $\frac{CLOUDY\ SB}{observed\ SB}$
CO (J=3-2)[2]	20	867.56	-5.20	-5.97	0.17
CO (J=4-3)[2]	14	650.70	-5.12	-5.86	0.18
HCO+ (J=4-3)[3]	14	840.94	-7.06	-8.27	0.061
Spitzer[4]3.6		3.6	-2.04	-3.29	0.057
Spitzer 4.5		4.5	-1.81	-3.24	0.083
Spitzer 5.8		5.8	-1.53	-2.94	0.062
Spitzer 8		8.0	-1.23	-2.41	0.062
Spitzer 24		24.0	-1.00	-1.53	0.30

[1] SB = surface brightness
[2] Data from Schuller et al. (2006)
[3] Data from White et al. (1999)
[4] All of Spitzer data taken from Spitzer archive

Table 2.4 shows the comparison between the observed data to the inputs of CLOUDY. The beam size of each data are shown in the second column of the table. For the Spitzer data, they were convolved to a comparable size of our HI data ($\sim$ 20"). The last column shows the ratio of the model to the observed. The observed quantities were converted to the units of surface brightness to be able to compare the values. For this current model, all of the spectral lines are underpredicted. For the strength of CO lines, we are aware, as mentioned earlier, that the current version of CLOUDY does incorporate the CO freeze-out however as a fixed values, as in it is not grain dependent. CO tends to freeze on to grains in cold ISM. Once a full CO freeze-out model is incorporated into the next version of CLOUDY, we will most likely see different result. In all of the Spitzer bands, we are underpredicting the emissions, yet we are missing the 12 μG and 13 μG PAH emissions from the Spitzer data as shown in Figure 2.11. The Spitzer telescope was constructed mainly to observe PAH emissions, and we only use the default size distribution of PAH in our model. If we change the size and/or abundance of the PAH, this result will be different. A better model for PAH emissions are still under investigation.

Our current model shows the likeliness of the physical conditions. a) It shows a very similar 21-cm optical depth, b) the maximum magnetic field is close to our upper limit, c) the stopping distance is within the predicted dimension of the cloud, and 4) the volume density is also in agreement with what is reported in White et al. (1999) who reports an existence of a molecular core at p_0 . If the magnetic field is removed from the current model but all of the other conditions are kept the same, then the total thickness of the cloud becomes about a half of the original prediction with the

35

magnetic field. This result seems understandable. The magnetic field contributes about half of the total pressure in the molecular gas. So when the magnetic pressure is turned off, the pressure drops by about a factor of two. To keep the total pressure the same, the model must increase the gas volume density by a factor of two. With twice the volume density, the specified stopping N(H) is reached in half the length. The conclusion we can draw from the non-magnetic-field model is that the magnetic pressure appears not to be a dominant effect in the pillar. In such case, the peak optical depth becomes about 0.65 . This can still be a very close to the actual values. However that is not to say that magnetic fields do not play an important role in a star-forming region. The study of Zeeman effect is a statistical study, and this is one result from one star-forming region.

Chapter 3 High Velocity Clouds

3.1 Introduction

High Velocity Clouds (HVCs) are interstellar clouds that hold anomalous radial velocities than what can be explained by the simple rotation of the Milky Way disk. 21 cm emissions can be observed almost in all directions in the sky. When the survey of 21 cm emission lines was conducted in the 1960's, astronomers have observed some peculiar clouds that had very different velocity components than what was expected from the galactic rotation. Their velocities were much higher than the clouds that are located in the galactic disk, therefore the name "high velocity clouds" stuck around. Today by definition, HVCs are the clouds whose velocity of local standard of rest (v_{lsr}) is greater than $\pm$ 90 km/s (Wakker and van Woerden, 1997). The LSR is the reference frame in which stars of the Solar Neighborhood have zero average vector velocity. Each star has its own "peculiar" velocity relative to the LSR, including the Sun. v_{lsr} is the measurement of radial velocity which uses solar neighborhood as the rest frame and also accounts for the peculiar motion of the Sun around the center of the Galaxy since the Sun does not orbit in a perfect circle.
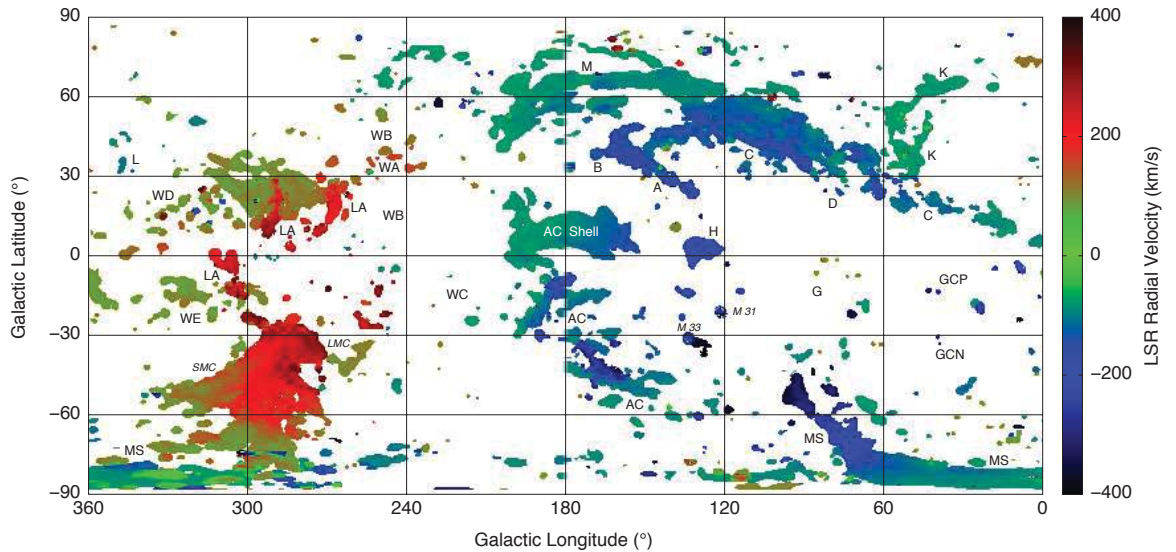
Figure 3.1: All-sky velocity map of HVC figure from Westmeier (2007), excluding the HI emission from the Galactic disk.

Figure 3.1 shows a distribution of the HI emissions which come from the HVCs. In this image by Westmeier (2007), the Galactic disk HI emissions are excluded for the purpose of showing only the HVC emissions. As can be seen, the v_{lsr} has a wide range of $-400 < v_{lsr} < 400$ km/s.

HVCs cover a large portion of the sky, as much as 40 % of the sky, mostly consist of neutral hydrogen and predominantly reside off from the galactic plane. A well-known example of HVCs is the Magellanic Stream which exists below the galactic disk. Its origin is thought to be from the material stripped away from the Magellanic clouds due to the tidal force. Other HVCs' origins may be from the residue from the formation of the Galaxy, the material which was once part of the galactic plane but were blown off by supernovae, the intergalactic material etc. Some of the clouds are considered unbound and unstable, especially those clouds falling towards the galactic disk. Some show evidence of interaction with the Galactic halo (Brüns and Mebold, 2004; Lockman, 2003).

Despite of all of that mentioned above, there are a large unknown facts about HVCs including their chemical contents, physical conditions, and their future prospects. Do HVCs even have magnetic fields? It is widely accepted that the average magnetic field in the galactic plane is about 2-4 μG and it is primarily parallel to the plane of the Galaxy (Han et al., 2006). However, we do not have a general understanding of the fields in the halo because there is significantly less material in the halo than the disk, which makes the detection of the fields much more difficult.

In this chapter, the fundamental questions that we ask ourselves are as follows. What holds the clouds together? Could it be magnetic field? What will happen in the future? In the process of searching for answers, the effects of magnetic fields are investigated since they may be the key component to stabilize the clouds and they may shed some lights on the magnetic processes in the halo.

3.2   Observations and Data Reduction

The HI observations were carried out over 4 periods of time using the 100m Robert C. Byrd Green Bank Telescope (GBT) in Green Bank, WV. The beamwidth is 9' with the central frequency of 1420 MHz. The number of the spectral channels per polarization was chosen to be 1024 with the Spectral Processor in full-stokes mode. Since GBT is made to observe linear polarizations simultaneously, those two linear polarizations were combined to create Stokes I and Stokes V, which are measured in circular polarizations. Below is a table of the time of observations, the observed sources, and their positions.

Table 3.1: Source Information

Time	Source Name	RA (J2000)	DEC (J2000)	Galactic longitude	Galactic latitude
Jan 2004	CasA	23:23:24	+58:48:54	111.73	-2.12
	HVC131+01_H1	02:02:49	+62:44:53	131.0	+1.0
	HVC132+23_A1	05:12:37	+80:48:38	132.0	+23.0
Sep 2004	CasA	23:23:24	+58:48:54	111.73	-2.12
	CHVC125+41_1	12:26:40	+75:31:12	125.34	+41.47
	CHVC125+41_2	12:27:40	+75:24:00	124.9	+41.63
	CHVC125+41_3	12:26:35	+75:30:00	125.0	+41.52
Mar 2006	CasA	23:23:24	+58:48:54	111.73	-2.12
	smith2	19:45:27	-01:18:00	38.00	-12.59
	halo1	18:03:50	-09:02:00	19.40	+6.28
	bootes1	12:24:00	+35:05:00	60.60	+68.7
Jan 2012	CasA	23:23:24	+58:48:54	111.73	-2.12
	smith2	19:45:27	-01:18:00	38.00	-12.59
	smithA	19:51:08	-01:00:10	38.94	-13.71
	smithB	20:06:32	+01:27:03	43.06	-15.94
	CHVC125+41_3	12:26:35	+75:30:00	125.0	+41.52

The first three observations were carried out by Tom Troland and the last January 2012 observing run's principal investigator was myself.

Cas A was observed for every observing run for the consistency check since it has a well known strong magnetic field, therefore we used it to assure that we applied the reduction software correctly to our results, as discussed in details later. For each time, it was observed for ∼ 1.5-2 hours.

Kazes et al. (1991) reported a magnetic field detection via Zeeman effect in HVC132+23-212 of $B_{los} = -11.4 \pm 2.4 \mu G$. It is this ground that the two positions, HVC131+01_H1 and HVC132+23_A1, were picked for this initial observation, in hopes of a) confirming the detection and b) magnetic field detection in other regions towards the this particular big complex of HVC.

The Compact High Velocity Clouds, CHVCs, are isolated, in both position and velocity, small HVCs whose angular size is less than 2 degrees in the sky, as defined by Braun and Burton (1999). CHVCs are generally regarded as a more distant populations, located typically within a few 100 kpc from the Milky Way (de Heij et al., 2002), than the general spatially extended HVCs. Some argue that they are associated with the Galactic halo (Maloney and Putman, 2003), and some argue that they may be a Local Group population (de Heij et al., 2002). Regardless of which model is correct, CHVCs are probes of physical conditions at considerable distant objects from the Galactic disk. Three positions, CHVC125+42_1, CHVC125+42_1, and CHVC125+42_1, towards the cloud were observed.

The Halo Cloud was previously mapped with the GBT and was reported to have a dense HI core, hence making the position, halo1, a potentially good candidate to carry out a sensitive Zeeman observation.

The Wave Cloud has been mapped in the past. Its galactic latitude is very high yet has an anomalous radial velocity at the latitude. In this region, most of the HI are approximately vertical to the galactic coordinates. The position of the interest, bootes1, is highly elongated which is part of the Cloud, and fairly bright in HI.

When the Smith Cloud was mapped (Lockman et al., 2008), its cometary morphology strongly suggests it is plunging toward the galactic plane. Interestingly, there were Hα and ionized nitrogen, NII detections (Bland-Hawthorn et al., 1998). This means that this cloud has been at least partially ionized by a nearby object. This cloud is expected to collide with the magnetized galactic disk in the future and is also modeled by Santillán et al. (1999); Santillan et al. (2001). Investigation of magnetic field toward this cloud may shed some light on the fate of the Cloud as well as the collision between primordial and processed gas. Initially the tip of the cloud, smith2, was observed.

The January 2012 observation trip was a follow-up of some of the targets that were previously observed. Before the observing run, we were able to reduce all of the previous data and were very confident that we had a magnetic field detection in the Smith Cloud, thus observed the same position to increase the coverage in the sky and also two other promising positions. After reducing the CHVC125+41_3 data, despite the small integration time, there was a strong apparent Zeeman detection, therefore we observed the same target that covers different hour angles (HAs).

Table 3.2: Observing Time

Time	Source Name	Integration Time [min]	Bandwidth [MHz]
Jan 2004	HVC131+01_H1	470	0.625
	HVC132+23_A1	740	0.625
Sep 2004	CHVC125+41_1	520	0.625
	CHVC125+41_2	485	0.625
	CHVC125+41_3	130	0.625
Mar 2006	smith2	625	2.5
	halo1	670	2.5
	bootes1	1180	2.5
Jan 2012	smith2	90	2.5
	smithA	510	2.5
	smithB	665	2.5
	CHVC125+41_3	580	0.625

The observations were carried in the frequency switching mode to maximize the

on-target observing time. The bandwidths used vary depending on the target source, therefore Table 3.2 shows the used bandwidth for each source.

The Zeeman observation using the single dish is fairly unique, therefore the data were reduced using the IDL package written and distributed by Carl Heiles and Tim Robishaw. The linearly polarized source 3C286 was observed for calibration purposes. The GBT spectrometer is capable of measuring all four Stokes parameters simultaneously. However, there is an inevitable "leakage" of signal for each parameter into every other parameter. For example, true Stokes I is equal to the observed Stokes I times a "leakage" factor, plus observed Stokes Q times another "leakage" factor plus the observed Stokes U times another "leakage" factor plus the observed Stokes V times a fourth "leakage" factor. A similar situation applies for the true Stokes Q, the true Stokes U and the true Stokes V. There are, therefore, a total of 16 leakage factors which make up a 4×4 matrix called the Meuller Matrix. This matrix must be determined by observations of a calibration source of known polarization characteristics. the matrix must then be applied to all of the program source data to convert observed Stokes parameters into true Stokes parameters. The Mueller Matrix coefficients were then calculated and applied to compose the correct IEEE definition of Stokes V (RCP - LCP) (Robishaw and Heiles, 2009). The calibration data was also reduced to evaluate beam squint, which is explained in details in the Discussion section. The details of the Zeeman dataset reduction are explained thoroughly in documentations provided by Carl. (How do you cite the documentation given by Carl ?) (Heiles and Troland, 2004). The correct sense of circular polarization was also calibrated and confirmed by reducing Cas A. The fitted magnetic field strength was $7.1 \pm 1.1 \mu$G at v_{lsr} = -48 km/s and $14.8 \pm 1.2 \mu$G at v_{lsr} = -38 km/s, which are accepted values from Verschuur (1969), which reports $9.2 \pm 2.6 \mu$G and $19.3 \pm 1.6 \mu$G respectively.

3.3   Magnetic Field Measurements

After the data has been calibrated correctly, the line-of-sight magnetic field strengths have been fitted using Eq. 1.12. The resultant field strengths are in Table 3.3 below.

Table 3.3: B_{los} Strengths and Errors

Source Name	B_{los} [μG]	B_{los} error [μG]
HVC131+01_H1	-0.2	0.8
HVC132+23_A1	-0.7	0.4
CHVC125+41_1	0.9	1.1
CHVC125+41_2	11.0	7.9
CHVC125+41_3	-1.7	0.6
halo1	-4.3	1.7
bootes1	2.2	0.8
smith2	-13.8	1.2
smithA	-8.1	2.2
smithB	-14.0	0.3

Although we found no significant magnetic fields in most of the regions, there seems to have been a significant detection towards the Smith Cloud, in all three positions, smith2, smithA, and smithB. Because of it, the Smith Cloud has become a primary focus of this project.

The Smith Cloud has recently been considered a HVC because of the large velocity component, +100 km/s, and lies well below the Galactic disk. The cloud is spread out a slightly larger than $10°$ in the sky at $\ell \sim 38°$ and $b \sim -13°$ and contains a few times 10^6 $M_\odot$. The brightest point in HI, with the column density of 5.2×10^{20} cm^{-2}, is at the tip of the cloud, the closest to the galactic disk. It sits about 3 kpc below the midplane of the disk, that is in the z-axis in the Galactic coordinates, and is reported that it is moving towards the disk and eventually will crash with cloud in the Galactic plane to spark a star forming burst in a few 10s of million years (Lockman et al., 2008).
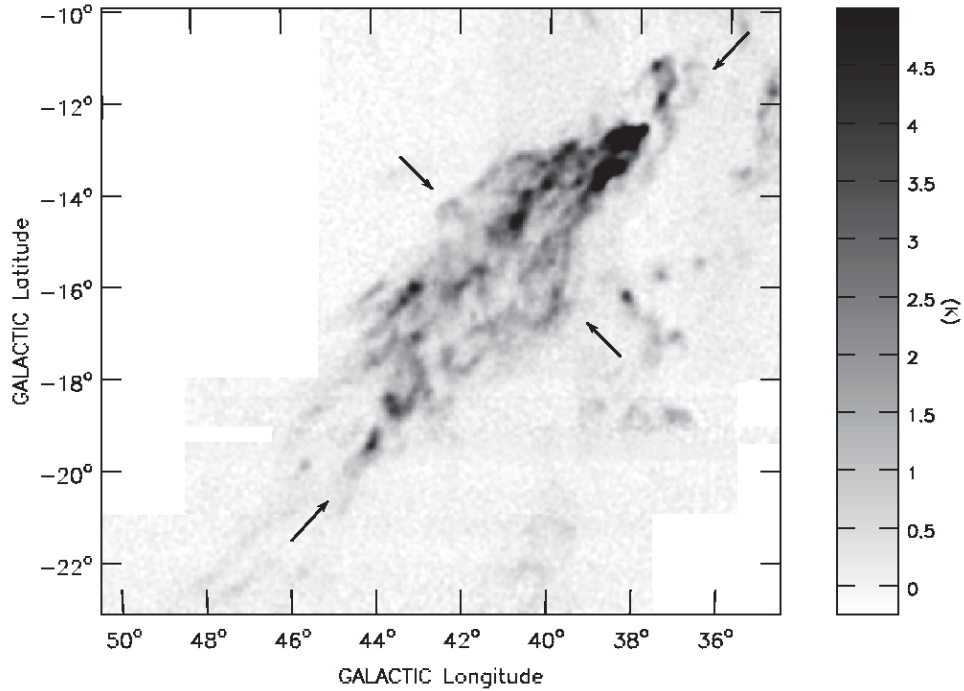
Figure 3.2: The Smith Cloud that was mapped by Jay Lockman using GBT. Figure 1 from Lockman et al. (2008)

From the morphology of the cloud and also kinematics, it is suggested that the cloud is interacting with an external medium (Mirabel and Morras, 1990; Brüns et al., 2000; Brüns and Mebold, 2004; Peek et al., 2007), most likely the ambient medium in the halo. If magnetic field is detected in the cloud, the density of the medium can be estimated by using the pressure equilibrium, which is discussed in details later.

3.4   Discussion

Before we conclude for a definite detection the Smith Cloud, there are a few analyses that need to be run on the Smith data. For a very long period of time, the HI observations using GBT have been thought to be a hard task because of the instrumental effects that the setup of the telescope creates along with what nature presents to us. Since initially there seems to be detection towards the cloud, we needed to look into the possible data contamination that comes from the instrumentation. To our best knowledge, we minimized the instrumental effect. The big question of " Is HI observation even possible with GBT?" on all of the Zeeman observers is answered.

When all of the data for smith2 are combined together, we get a following Stokes I, V and fitted field value.
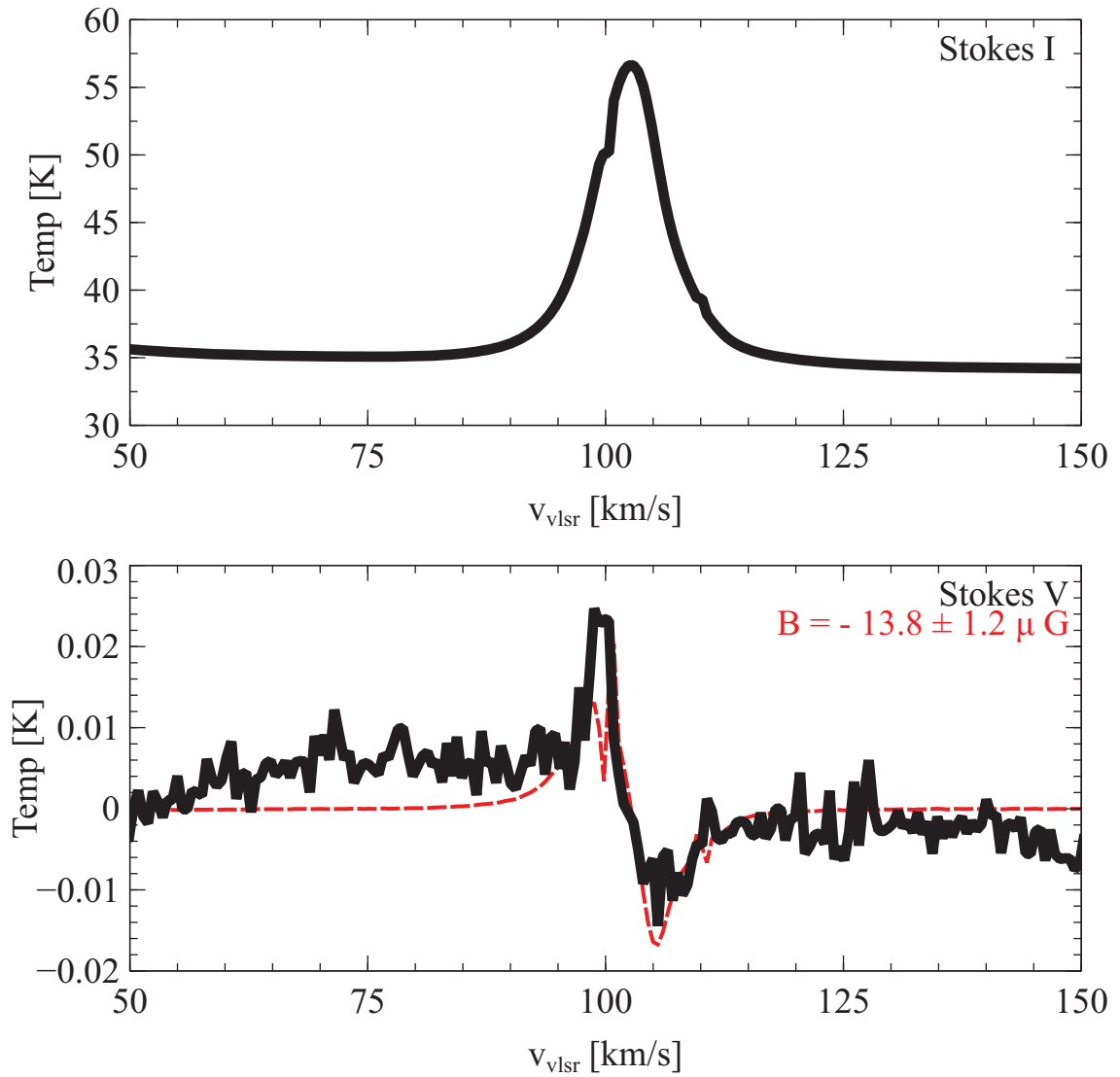
Figure 3.3: B_{los} of smith2 for all data.

The first order analysis to examine how much the data are changed because of the instrumental effect is to divide the data into East and West then measure the fitted field value.
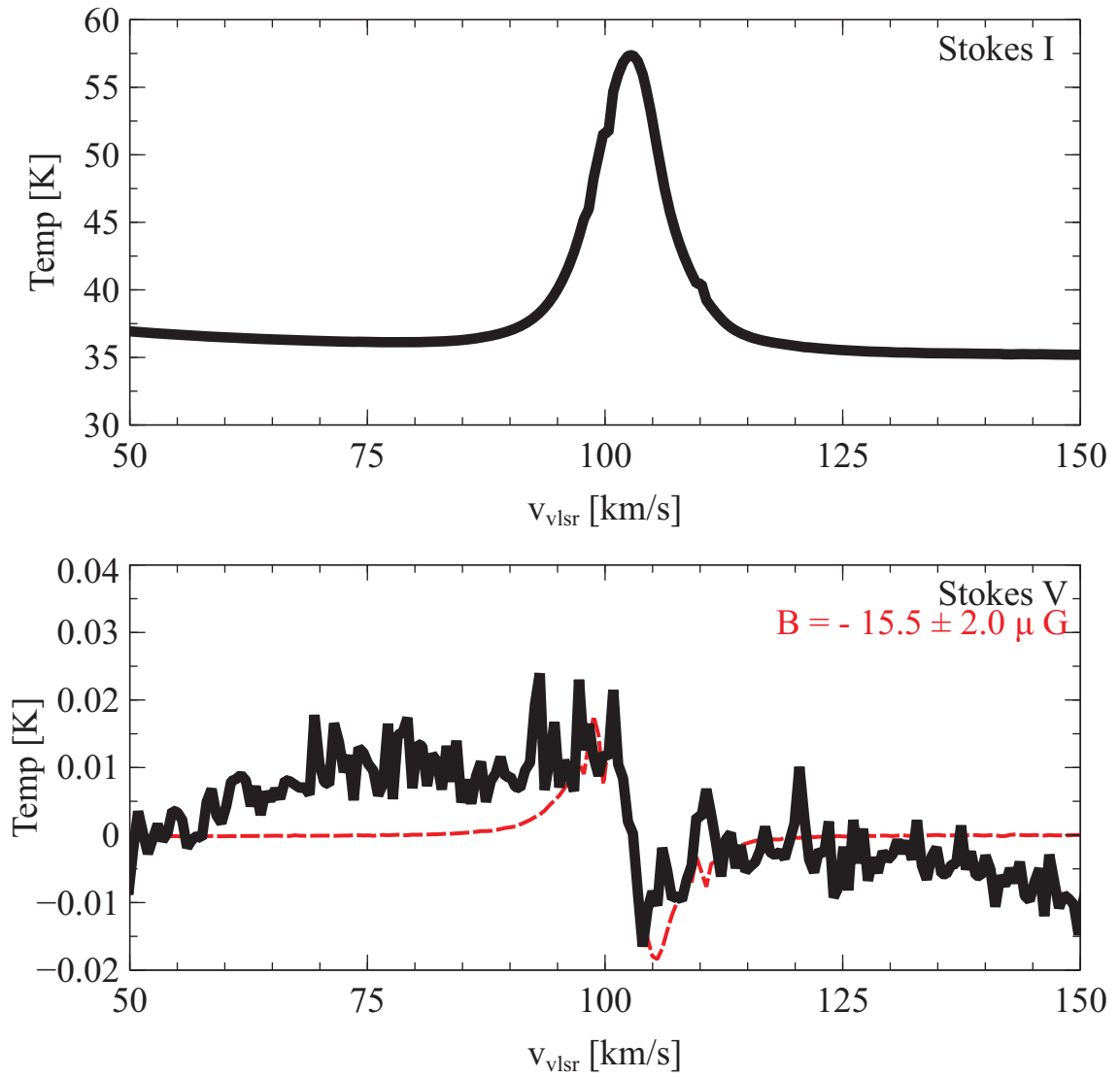
Figure 3.4: The fitted B_{los} for the west dataset of smith2.
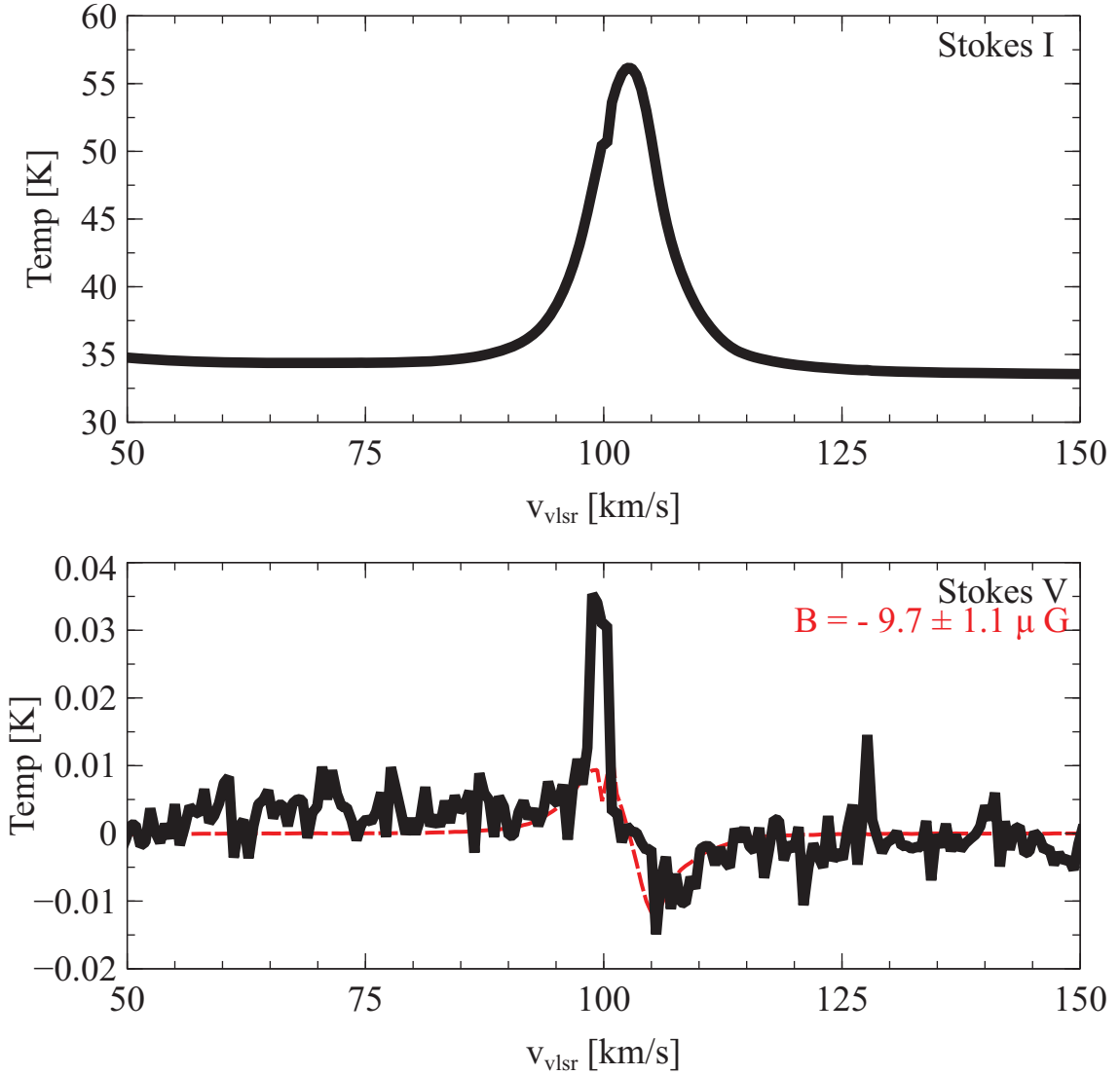
Figure 3.5: The fitted B_{los} for the east dataset of smith2.

Even though the fitted values do vary between the east and west data sets, the fitted values of $B_{los,west} = -15.5 \pm 2.0$ μG and $B_{los,east} = -9.7 \pm 1.1$ μG are comparable to each other and also with the all data combined. Also, the amplitudes of Stokes V are also very close to each other, which lead us to believe that at least the instrumental effect that comes from the combination of beam squint and velocity gradient are minimal.

3.4.1 Instrumental Effect: Z17 Analysis

What is exactly the instrumental effect which is due to the combination of beam squint and velocity gradient? When we do a Zeeman observation, there are two antennas that are sensitive to orthogonal polarizations and they operate simultaneously. For

single dish such as GBT, the two antennas may not be looking exactly at the same place, which is called "beam squint". The expression in French for beam squint is the equivalent of "cross-eyed". This meaning is relevant since the telescope is looking in two slightly different directions when observing the two circular polarizations, much like a crossed eyed person looks in two slightly different directions. Beam squint is natural and is expected to occur when the axis of the feed is tilted respect to the axis of the antennas. However, it becomes a problem if a target has a velocity gradient. When this situation occurs, the observed Stokes V may be contaminated by this particular instrumental effect. If $\Delta \vec{v}$ is the velocity gradient vector, and $\vec{\theta}$ represents the beam squint vector, the Stoke V that solely comes from instrumental effect is

$$\Delta \vec{\theta} \cdot \Delta \vec{v} = \text{Stokes V}_{\text{instrumental}} \tag{3.1}$$

From personal contacts with Carl Heiles, who also wrote the reduction and the instrumental effect calculation software package, we know that the instrumental effect is significant enough to pay close attention to. The observed points are plotted in Figure 3.6 below. Beam squint responds to the first derivative of the beam pattern, and the second derivative effect is called " beam squash" in Robishaw and Heiles (2009) but there was no instrumental Stokes V from the beam squash in our data, therefore the analysis was proceeded without taking into consideration.
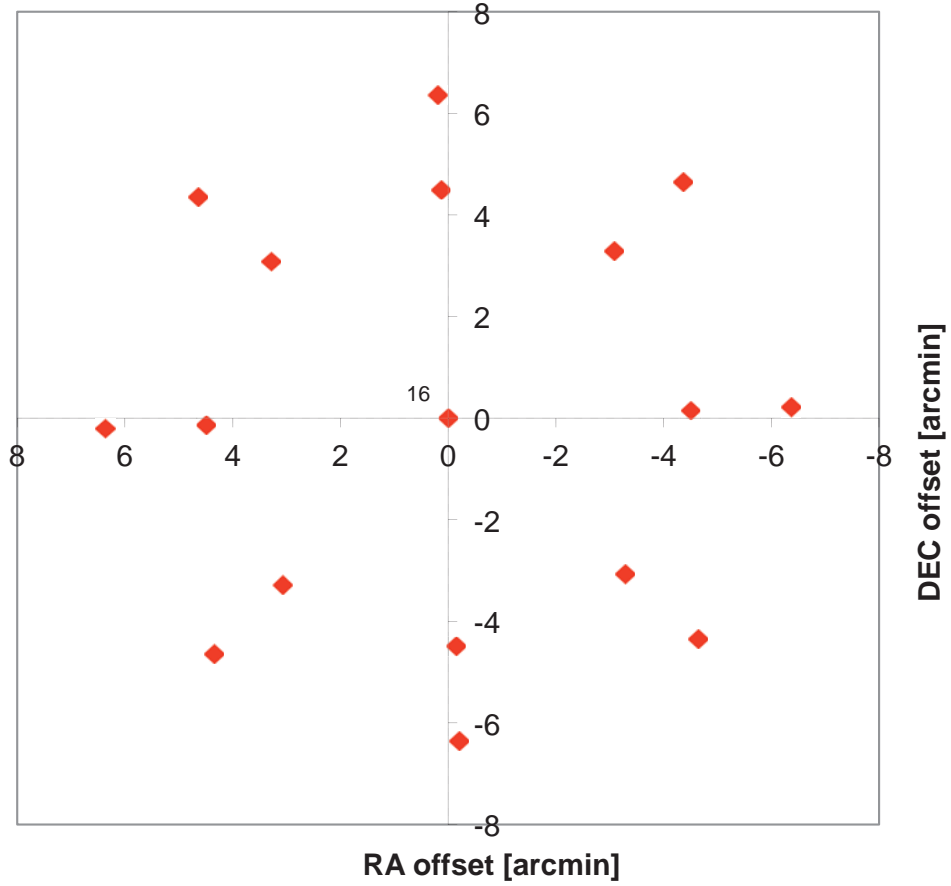
Figure 3.6: Z17 Pattern in the sky. The inner points are 4.5' away from the central position, which is a half of beam size. The observed points make two circles around the target, which each position is 45° apart.

When GBT is used for Zeeman observations, the observer must consider the beam squint contribution of the observed Stokes V before fitting the magnetic field. The beam squint in Stokes V, $\vec{\theta}$, which consists of a beam squint magnitude and angle, is thought to be a function of zenith angle shown in the Figure 1 of Robishaw and Heiles (2009). In the figure, both the magnitude and the angle of the beam squint are plotted up to ZA $\sim 40°$ and this is due to the duration of the calibration source observation. Then a Taylor series is fitted down to the 5th degree polynomial to express the squint as a function of ZA . With further investigation, we have realized, by determining the beam squint from various observing runs, that as the zenith angle increases the magnitude gets larger but the angle flattens out at roughly 150°. Especially for the beam squint, to fit the Taylor expansion more accurately, we used dataset whose calibration source observation was the longest, which was taken in August 2003, not from the HVC Zeeman observation runs of March 2006 nor January 2012 (See Appendix B in page 62 for details).

In order to check for the velocity gradient, we took spectral observations on 16

points around the source and 1 point on the source. The theory behind the observations is as follows. We calculate a velocity gradient in the vertical component by subtracting a North point profile from a South point profile and subtracting from West point to South point for the horizontal component, and combine them together to create $\vec{v}$ to determine the vector on the target. As seen in Figure 3.6, with the right combination we can estimate two components of velocity gradients that are orthogonal to each other. Therefore, a velocity gradient vector $\vec{v}$ in Equation 3.1 can be calculated.

With the velocity gradient and the beam squint as a function of ZA, the instrumental contribution to the observed Stokes V was calculated per scan. This is called the Z17 analysis, which is crucial to Zeeman observations with single dish telescope. The Z17 analysis is included in the IDL procedures provided by Carl Heiles and some details are also explained in Robishaw and Heiles (2009). Ideally we hoped that once the instrumental Stokes V have been averaged over all the scans, we would see minimal effect since we observed the sources for a long period of time to cover a great range of hour angles with the intensions of the effect being averaged out.
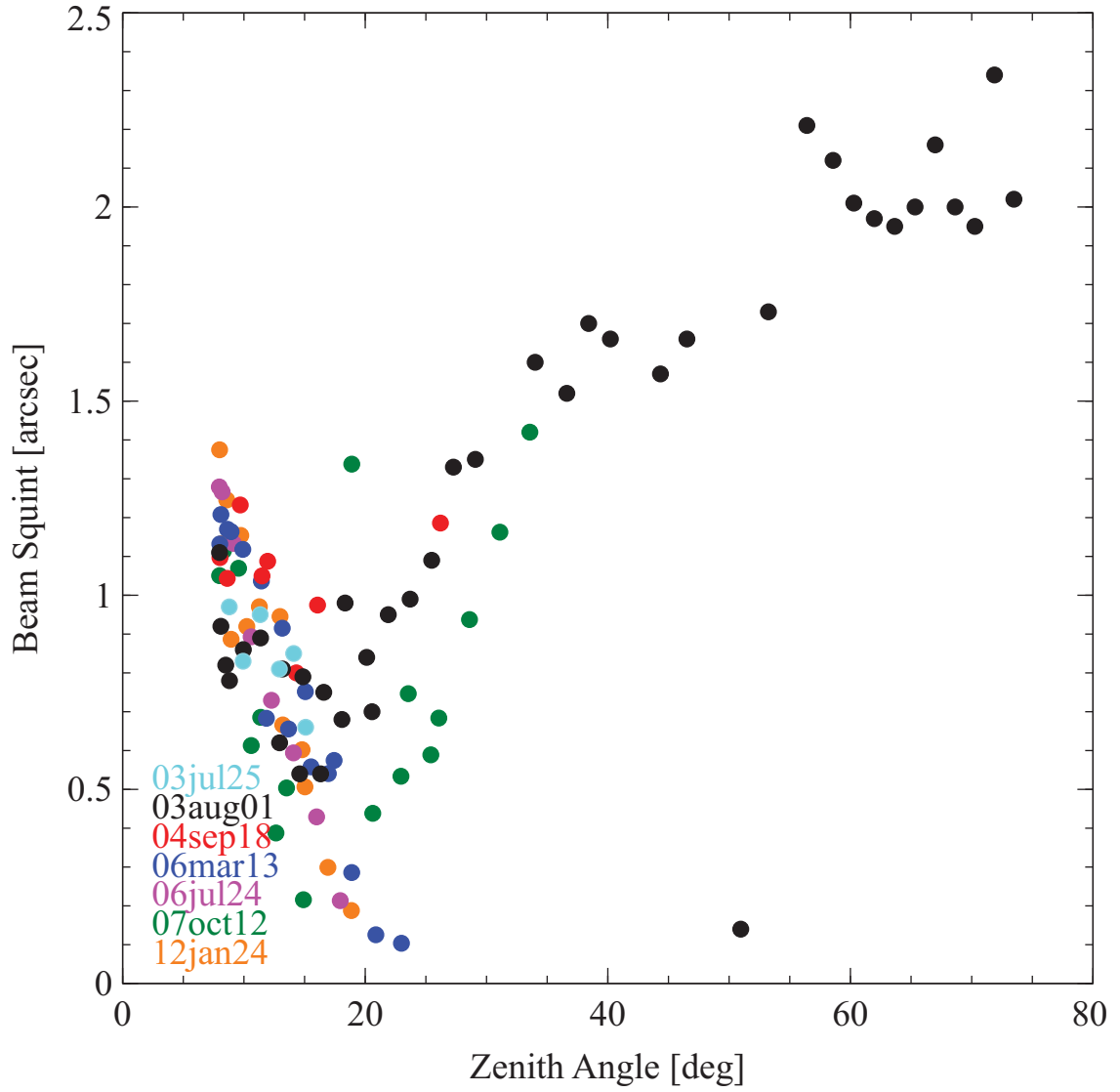
Figure 3.7: Beam squint values of 21cm from various observation times at GBT
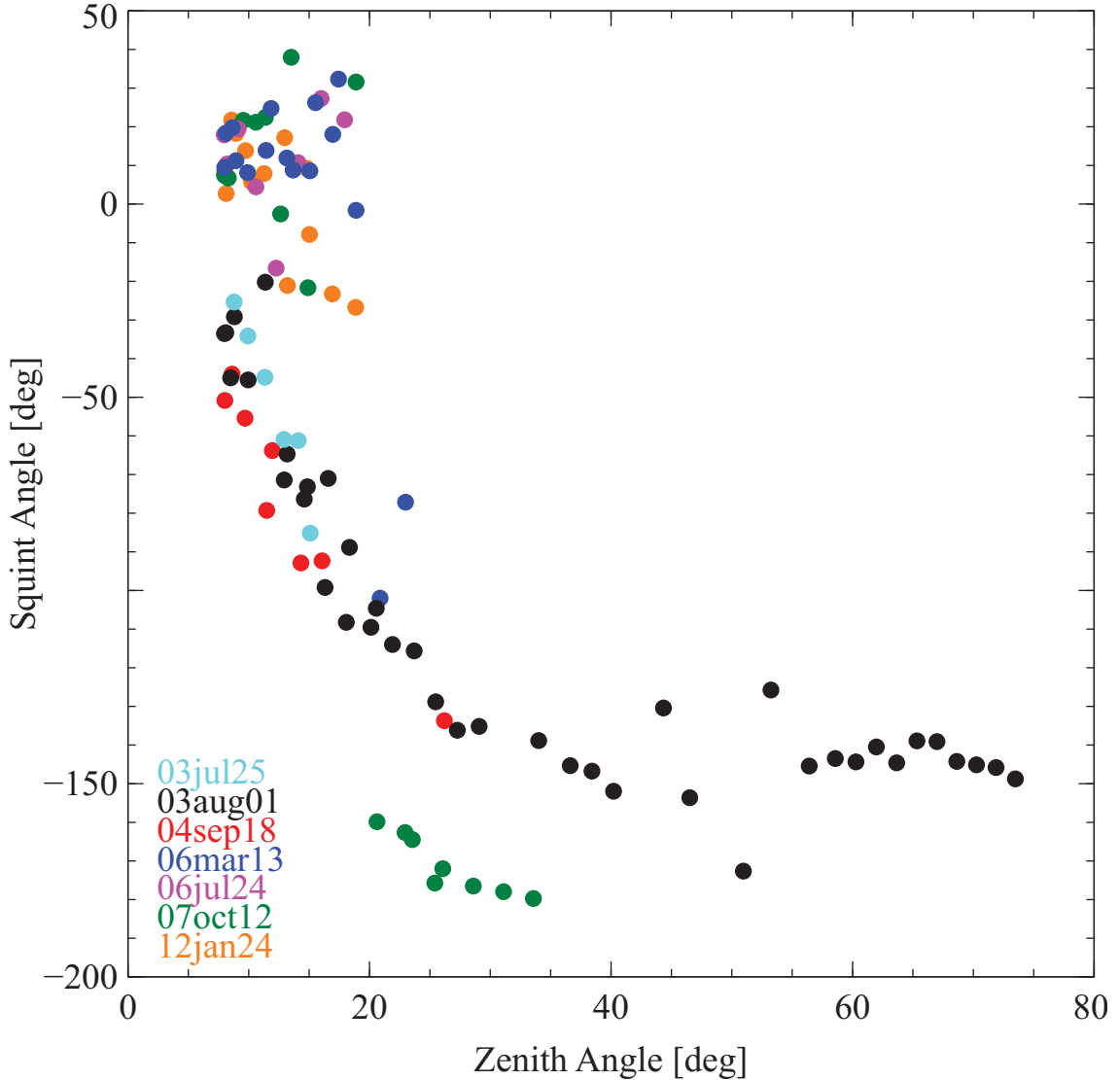
Figure 3.8: Beam squint angles of 21 cm from various observation times at GBT

We have assembled a variety of 21 cm GBT beam squint measurements made in the time frame 2003 to 2012. These measurements were made on 3C 286 with spider scans, which is an observational technique to measure the beam squint and angles. Figure 3.7 shows beam squint magnitudes in arcseconds, plotted with different symbols to represent different dates upon which the spider scans were taken. Similarly, Figure 3.8 shows the beam squint angles. Note that only data taken on 01-AUG-03 cover zenith angle, ZA, > 35 degrees. Since smith2 has a great ZA coverage, in order to calculate the beam squint contribution, we decided to use the 01-AUG-03 spider scans. The Heiles Z17 software calculates the expected instrumental contribution to the Stokes V profiles owing to beam squint. Beam squint is assumed to be a function of ZA. The five-degree Taylor series coefficients are used by the Z17 software to compute the beam squint magnitude and angle for each Zeeman scan, based upon

the ZA of that scan.
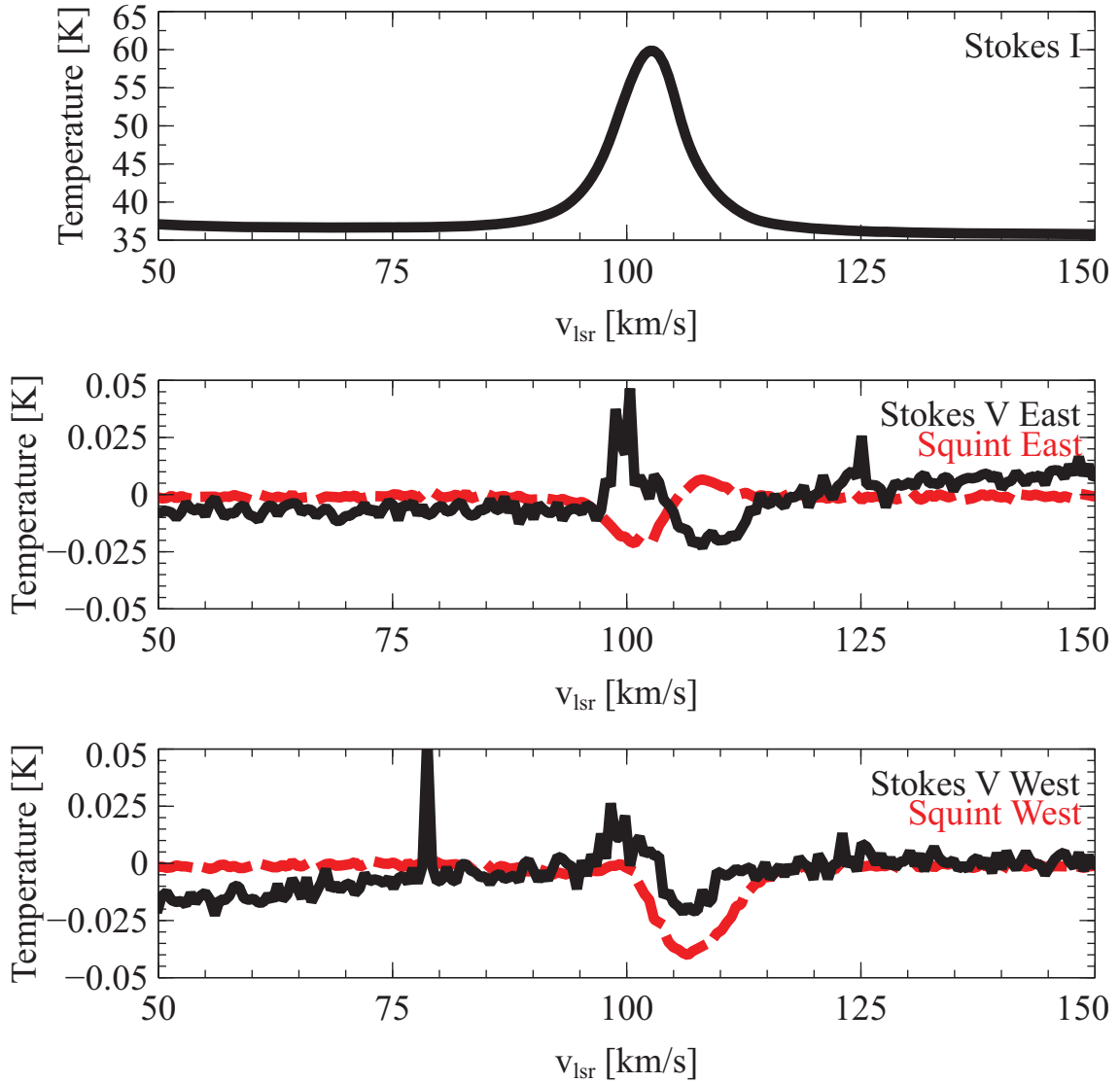
Figure 3.9: Smith2 beam squint calculation with the Z17 software. The top figure shows Stokes I, the middle one shows Stokes V in solid line and calculated squint contribution in red dashed line of the East, and the bottom one shows Stokes V in solid line and the red dashed line is the squint contribution of the West data.

The Figure 3.9 above shows the beam squint calculation when the data were split into the East and West subset. The dashed lines shown in the middle and the bottom plots of this figure show the calculated squint contribution to Stokes V. As clearly seen, the beam squint contribution to the East creates an opposite S curve to both the observed Stokes V in Figure 3.5 and also the observed Stokes V in Figure 3.3 when all of the data are combined. The squint result in the East data were unexpected since, assuming that the magnetic field detection is real, a) the magnetic field does

52

not vary when the source is observed at different times and b) comparing all three figures of Stokes V from Figures 3.3, 3.4, and 3.5, they all have the same sign of the S curve.

We have then re-computed the instrumental Stokes V profiles for East HAs and for Eest HAs separately, assuming constant (i.e. ZA-independent) values for the beam squint magnitude and angle, independent of the Z17 software. In changing the squint angle from (e.g.) -130 to -80 degrees, we found the sign the instrumental Stokes V changed for the East HAs and for the Eest HAs. Note that this range in angle is reasonable given the variations shown in Figure 3.8. We conclude that the imprecision with which we know the beam squint magnitude and angle for each Zeeman scan renders the calculation of instrumental Stokes V profiles quite uncertain.

It seems as though that the beam squint magnitudes and angles are not strict functions of ZA. The GBT beam squint must be a function of parameters other than ZA, perhaps azimuth and/or time or even physical temperature of the telescope. In light of these uncertainties, it is not possible to calculate beam squint contributions to Stokes V profiles with high accuracy. There are other tests that we will need to explore on the beam squint issue. Thus, we will continue the investigation but we are very confident that the magnetic field result is a true detection, that it is not all instrumental because we obtain very nearly the same field value in the east HA scans as in the west HA, over a parallactic angle range of nearly 100 degrees.

3.4.2 Instrumental Effect: Sidelobe Contribution

The importance of the paper Robishaw and Heiles (2009) not only deals with the instrumental effect on Stokes V but also with the contamination to Stokes I from distant sidelobes. The way the GBT telescope is set up is such that it catches stray radiation that come from the background radiation. This happens outside of the main beam, named the sidelobes, which Robishaw and Heiles identified contribution that comes from three components that make contribution; 1) the spillover ring, 2) the Arago spot, and 3) the Screen component. When there is sidelobe contribution to Stokes I, what needs to be investigated further and more carefully is the sidelobe effect to the observed Stokes V. If the stray radiation is polarized, then the sidelobe can affect the observed V. However, we need to take the step of this investigation only if there is significant contribution to Stokes I.

The spillover ring is due to the reflection caused by the secondary reflector of the telescope. The spillover ring is created 20 degrees off from the point of observation and peaks at roughly 5 degrees outside of the edge of the ring. The Arago spot is a bright spot that appears due to diffraction nature. The screen is mounted in such way that spillover radiation is deflected away from the main beam into the sky. However, unfortunately this deflected radiation gets caught as part of the spillover and can also contaminate the observation.

The sidelobes effet is particularly problematic in HI observations since the 21 cm emission is everywhere, especially towards the galactic plane. This issue of catching stray radiation was known long before we embarked on the project. However, since most of HVCs are far off from the disk, at least on the ones that we observed, also

have very different velocity components. Therefore if this type of H I observation were at all possible with GBT, HVCs would have been a perfect candidate for it. Nonetheless, as seen in Figure 4 in Robishaw and Heiles (2009), because the sidelobes effect can come from as far as 20 degrees off from the point of observation, we needed to check the scale of contamination from the sidelobes effect. Heiles mentions that if the sidelobes are polarized for some reason, the effect not only contaminates Stokes I but also V.

For this purpose, again we relied on Heile's effort and reduction software. This software uses the wide range Leiden/Argentine/Bonn (LAB) Survey of Galactic HI whose velocity coverage is from -450 km/s to 450 km/s at a resolution of 1.3 km/s. The software calculates approximate model of the sidelobes and the level of contamination to Stokes I separately that come from the three components mentioned above.

The West and East smith2 data were analyzed using the reduction routine. The scale difference in the y-axis comes from the difference in beam size of the survey and GBT. HPBW is 36' while GBT has 9'.
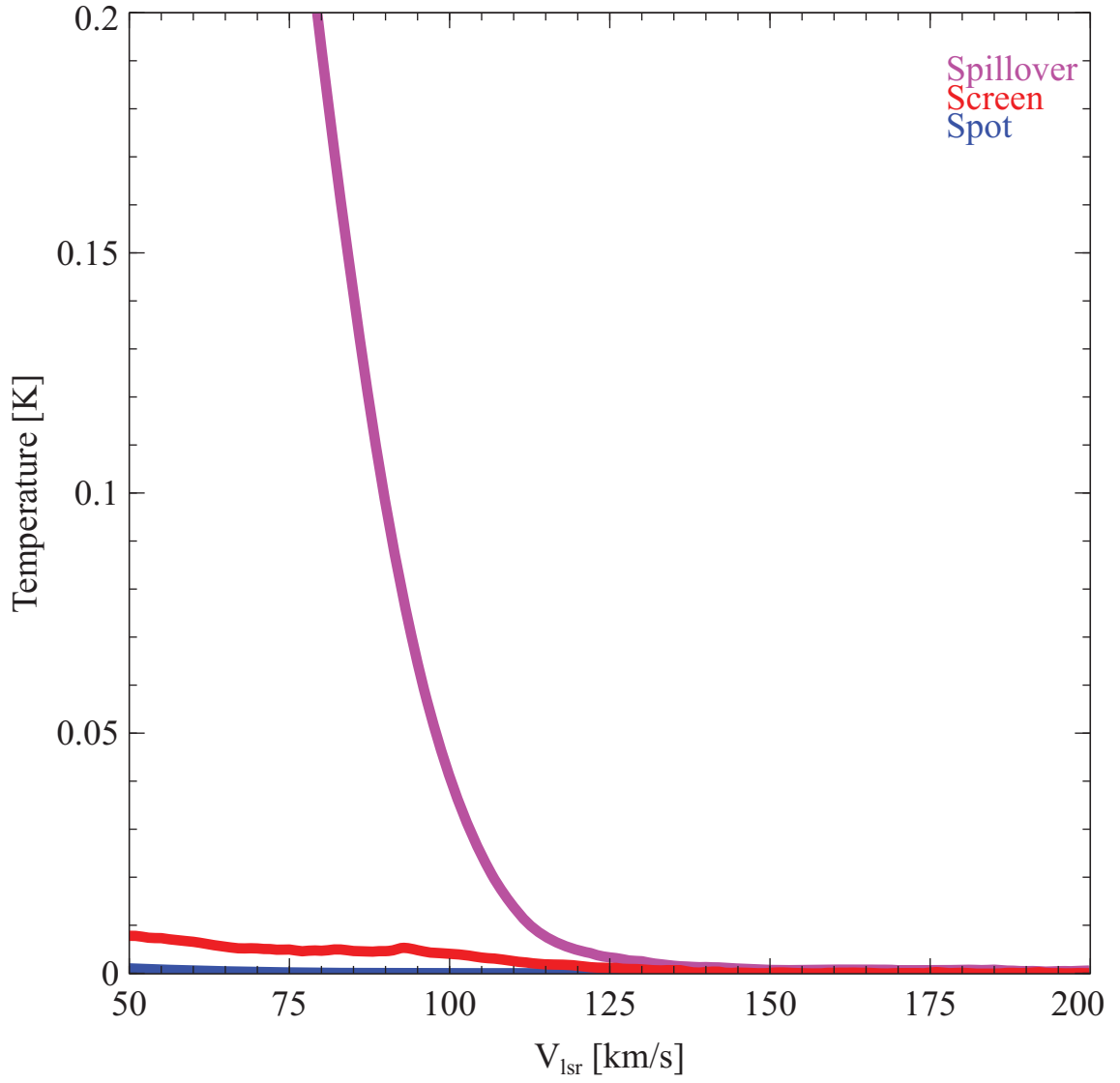
Figure 3.10: Sidelobe effect estimation in the West
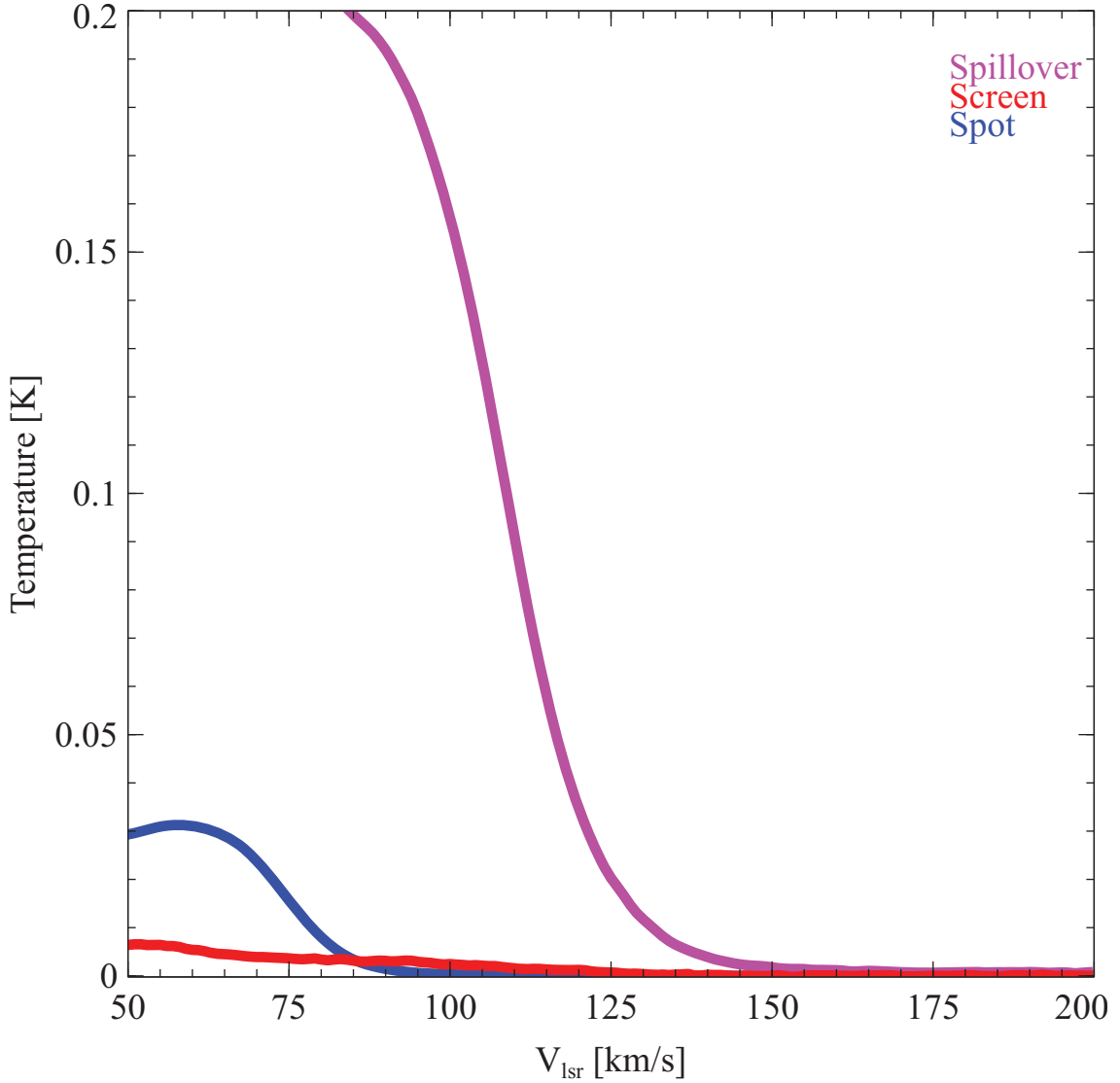
Figure 3.11: Sidelobe effect estimation in the East

The Figures 3.10 and 3.11 show the calculated sidelobe effect towards smith2. The peak emission that comes from smith2 is at $V_{lsr} = 102$ km/s. The spillover ring contribution dominates the Arago spot and screen components at all velocities, but also at the position. From this estimation, the Arago spot screen contributions near the Smith Cloud velocity are negligible since the amplitudes of those components in Stokes I are much smaller than the Zeeman effect (Figures 3.4 and 3.5). Also going back to those Zeeman effect figures, the fact that they are comparable, despite the fact that the predicted contribution of the spillover ring to the Stokes I is much greater in the East, must mean that the spillover effect in Stokes I make little-to-no contribution to the Zeeman data. Also, from the sidelobe estimations, there are no spectral feature in the spillover ring profiles in the West nor East. Therefore, it seems very unlikely that the spillover ring component could create an apparent Zeeman effect

in the Stokes V profile that very closely coincides with the Smith Cloud velocity.

Towards the Smith Cloud, there are also two positions, smithA and smithB, we carried the Zeeman observations to. Even though we have not run the sidelobe calculations on those positions, it is very unlkely that the reported Blos detections in those positions are completely instrumental. SmithA and smithB positions are very close to smith2, only a few degrees off at the maximum, when the spillover ring effect comes from 20 degrees, thus there should not be any spillover effect that cout contaminate the final results. Also it is important to note that all three positions show comparable results in Table 3.3.

3.5   Results

The very big question of whether the HI observation at GBT was possible, due to a number of instrumental effects, is partially answered. From our current results, the HI observations are possible, but only in the case of objects like High Velocity Clouds, there the sources are away from the Galactic center and have peculiar velocities than the normal Galactic rotation.

Despite the possible instrumental contamination to the observed data, we are confident that the magnetic field results shown in Table 3.3 are real. Of those detections, we are particularly interested in the Smith Cloud result.

Lockman et al. (2008) mentions that the Smith Cloud is co-moving at 130 km/s, respect to the velocity of the Galactic ISM, while the line-of-sight velocity is at 100 km/s. Our detection of magnetic field is towards the line of sight. Since the Cloud is piercing through an ambient medium towards the Galactic disk at 300 km/s respect to the non-moving frame, called the total space velocity, it can be assumed that the magnetic field at the tip of the cloud is clamped locally making the field strength bigger than the general magnetic fields in the Halo. The total magnetic field then should be pointing along the direction of the total space velocity. The total magnetic field is related to B_{los} by Eq. 2.6, which can vary depending on the angle between B_{los} and B_{tot}. From the cometary shape of the cloud piercing through the ambient medium, at the tip of the cloud, the pressure equilibrium between the internal and the external of the cloud is an appropriate assumption such that,

$$P_{mag} + P_{turb} = P_{medium} \tag{3.2}$$

where P_{mag} and P_{turb} are the magnetic pressure and turbulent pressure inside the cloud and P_{turb} is the pressure of the ambient medium in the Halo. Eq. 3.2 then becomes

$$\frac{B^2}{8\pi} + \rho_{smith} v_{line}{}^2 = \rho_{medium} v_{ISM}{}^2. \tag{3.3}$$

In this case B is the total magnetic field, ρ_{smith} is the density of the Smith Cloud, v_{line} is the line width, v_{ISM} is the velocity of the Cloud in the co-moving frame respect to the Galactic ISM. From this equation, density of medium in the Halo can be estimated.

Table 1 of Lockman et al. (2008) gives some of the useful properties towards the tip of the cloud. Note that these values are not exactly at the position of smith2, but rather where the column density was the highest in the region, thus the values may not be exactly correct for smith2. Nonetheless, we expect that the values are not going to be very different. The position for the values listed in Table 3.4 and smith2 are roughly 0.8° apart.

Parameter	Value
Distance	12.4 ± 1.3 kpc
z	$- 2.9 \pm 0.3$ kpc
T_b	15.5 K
Δv	16.0 km s^{-1}
N_{HI}	5.2×10^{20} cm^{-2}

Table 3.4: TABLE 1. of Lockman et al. (2008): HI Parameters of the position $\ell = 38.67°$ and $b = -13.42°$, which is close to the position of smith2

Towards the leading tip, also towards the position of smith2, If the brightness are plotted an imaginary perpendicular slit to the axis of the cloud and the half power width were measured, such plane-of-the-sky thickness of the cloud is equal $\sim 0.4°$, which makes the linear dimension of 2.7×10^{20} cm given the values from Table 3.4. The reasonable assumption here is that the line-of-sight depth of the cloud at the position of our interest is also in the same length scale as the linear plane-of-the-sky dimension, which makes the cloud volume density to be

$$\rho_{\text{smith}} = \frac{\text{N(HI)}}{\ell} \approx 2.0 \quad \left[\frac{\#\text{Hatoms}}{\text{cm}^3} \right] \tag{3.4}$$

which makes the turbulent pressure to be $1.2 \times 10^{-11} \left[\frac{\text{dyn}}{\text{cm}^2} \right]$.
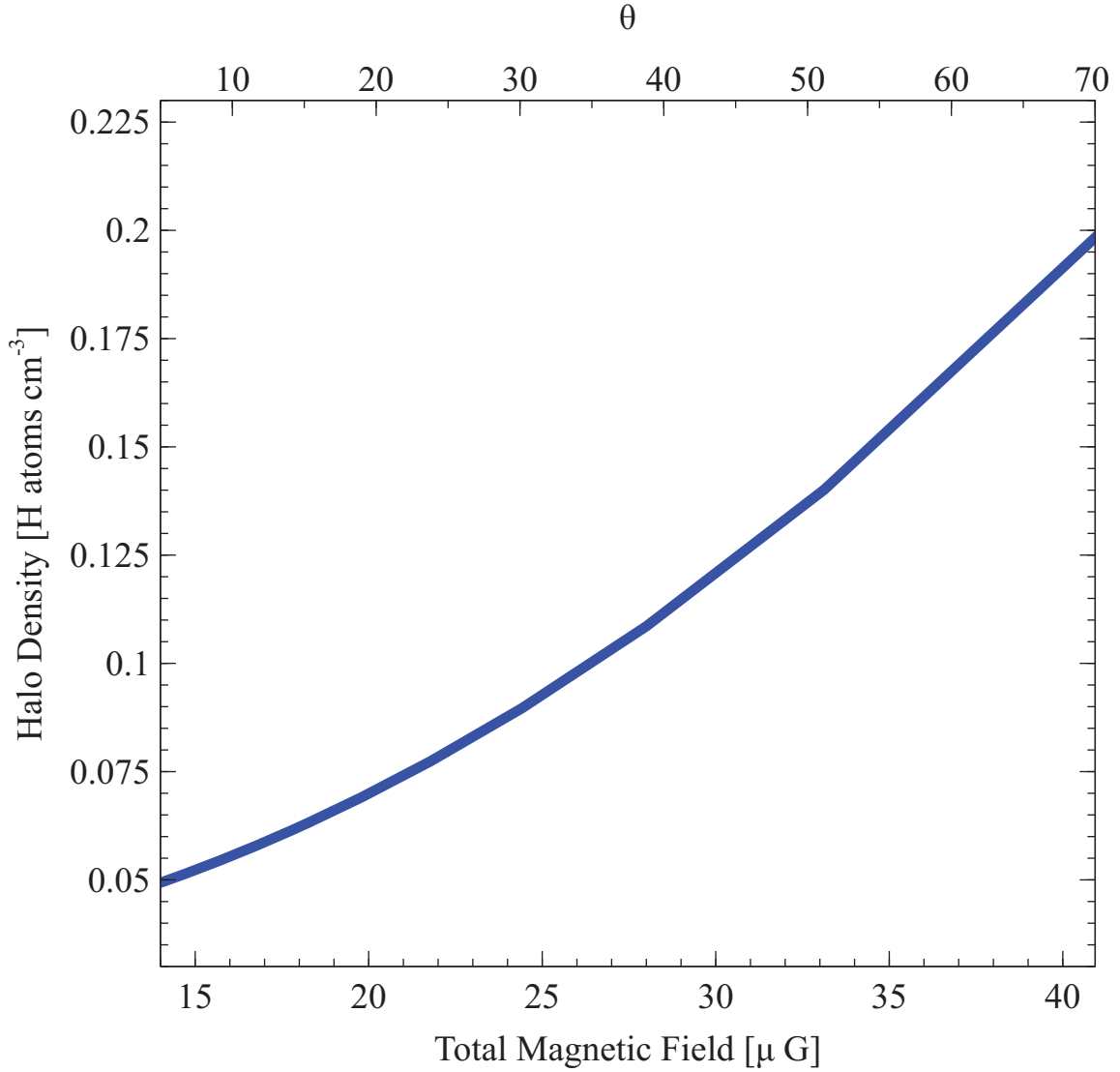
Figure 3.12: Halo volume density plotted as a function of total magnetic field

By computing the turbulent pressure and filling in the Equation 3.3, the Figure 3.12 above, the halo volume density is shown as a function of the possible total magnetic fields where the angle, θ, is varied from 5 to 70 degrees in the Equation 1.12.

Figure 3.12 shows the minimum Halo density of 0.05 hydrogen atoms per cubic centimeters and it may go up to as much as 0.2. Kalberla (2003) creates a model to describe the dark matter halo of the Galaxy and there they estimate the neutral and hot halo medium density to sit at roughly 4 kpc away from the mid-plane of the Galactic disk with a density of 1.2×10^{-3} cm^{-3}.

The typical density cold ISM neutral non self-gravitating atomic gas is around 50 hydrogen atoms per cubic centimeters while the warm neutral gas has a density of 0.1 hydrogen atoms per cubic centimeters. These possible values shown in Figure 3.12

for the density are assumed to be the upper limit of the medium since a) the column density at smith2 may be lower than what is used in the estimate, b) the actual B_{los} may be lower when more extensive instrumental effect calculations are performed and applied, and c) the line-of-sight depth of the cloud may not be 2.67×10^{20} cm. Despite of some uncertainties, we are very confident that this is a valuable value since there has not been a density measurement of the Halo. This is the first time the magnetic field was detected in the Smith Cloud and also the upper limit of the halo density has been placed based on the observational result.

Appendix A: Fourier Transform of Aperture and Beam

When a beam pattern is measured in the real sky coordinates, in the (x,y) in centimeter, for example, coordinates, we consider the corresponding *spatial frequency* coordinates, in the (u,v) coordinates in wavelengths. They are related by as follows.

$$u = \frac{x}{l} \tag{A.1}$$

$$v = \frac{y}{m} \tag{A.2}$$

where l and m are the angular separation on the sky. Therefore the measured pattern needs to be Fourier transformed to get the (u,v) radiation pattern with "voltage" distribution in the aperture.

Each interferometer measures a two dimensional brightness distribution of the source. What we would want is the corresponding intensity measure in the wavelength coordinates. In order to process the real 2D sky brightness to 2D intensity map is to Fourier transform the observed brightness into the spatial frequency dependent intensity. When the process is taken over, the beam pattern is also Fourier transformed, which creates a beam pattern which has a diffraction pattern.

$$F(l,m) = \int \int f(u,v) e^{2\pi(ux+vy)} du dv \tag{A.3}$$

Appendix B: Polynomial Fit

To calculate a function that best describes the beam squint magnitude and angle, a Taylor function of ZA is fitted.
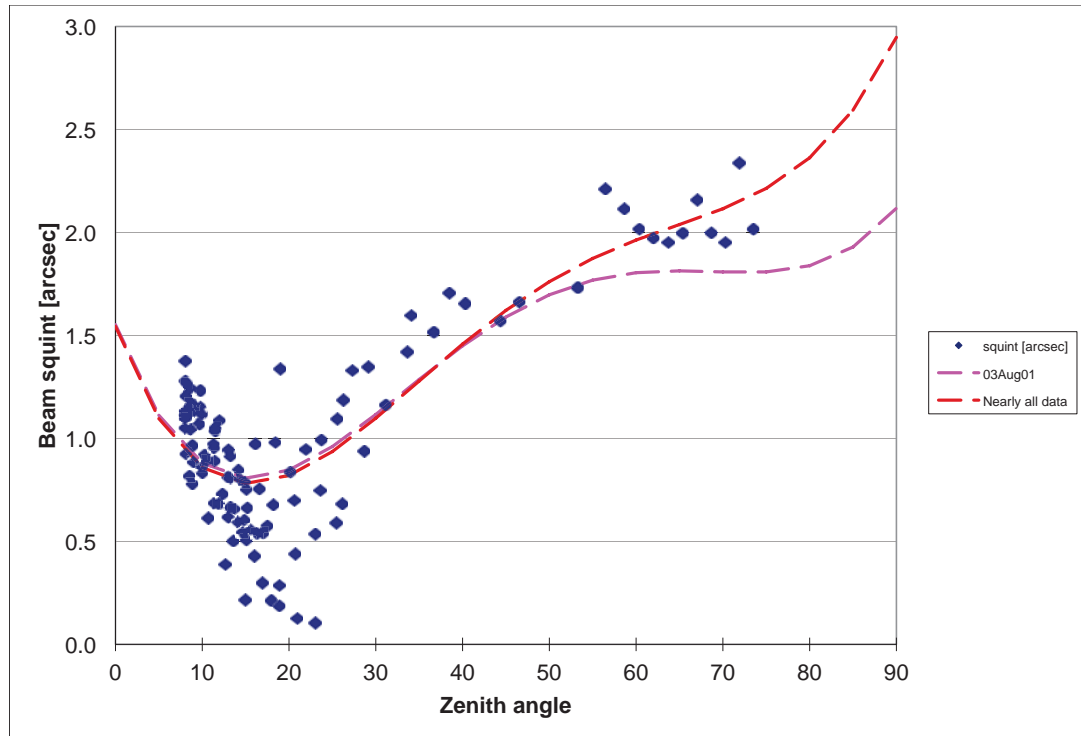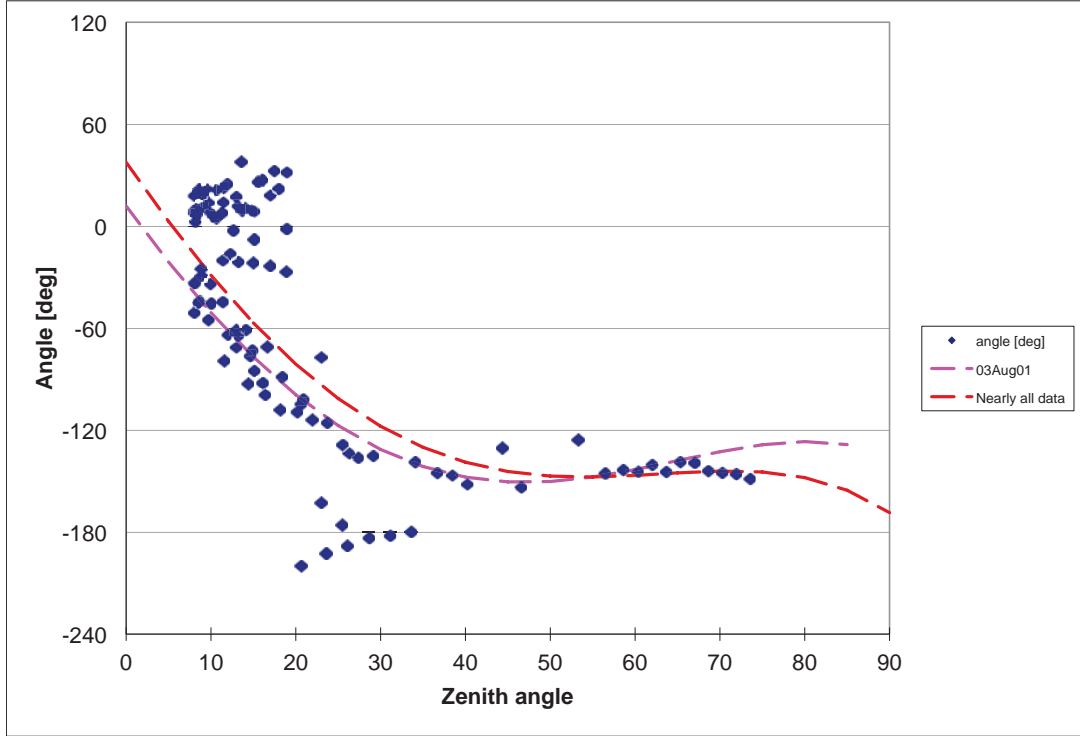

Figure B.1: Beam Squint Fit

Figure B.2: Beam Squint Angle Fit

Figures B.1 and B.2 show different derived 5th Polynomial coefficient fits to all of the calibration source data, 3C286, from the observations from 2003 to 2012. The blue dots represent all of the data points shown in 3.7 and 3.8 with some bad data points taken out. The pink dashed line, "03Aug01", represents a fit to the blue dots where the coefficients were derived only from the 01-AUG-03 observation. The red dashed line, "nearly all data", represents a fit to the data with the Polynomial fit derived from all of the blue dots. As can be seen from Figure B.1, all of the fitted lines are fairly close in ZA < 50 degrees but show different representation of the squint magnitude at higher ZA. From the squint angle fit from Figure B.2, all of the fitted lines are very close to each other but the "03Aug01" line seems to show a better fit to the data points the best. This is one reason that we decided to use the set of coefficients that were derived from 01-AUG-03. Another reason for choosing it is that this is when the source was observed with the widest range of ZA, hence best represent the actual observation as well. Note that some of the data points are not close to the fitted lines, especially for ZA < 30 degrees. Thus, as mentioned, we think that the beam squint may not be the only function of ZA, but possibly also a function of azimuthal angle or maybe even time.

Bibliography

Bland-Hawthorn, J., Veilleux, S., Cecil, G. N., Putman, M. E., Gibson, B. K., and Maloney, P. R. (1998). "The Smith cloud: HI associated with the SGR dwarf?". *MNRAS*, 299:611.

Braun, R. and Burton, W. B. (1999). "THE KINEMATIC AND SPATIAL DEPLOYMENT OF COMPACT, ISOLATED HIGH-VELOCITY CLOUDS". *A& A*, 341:437.

Brogan, C. L. and Troland, T. H. (2001). "VLA H I AND OH ZEEMAN OBSERATIONS TOWARD M17". *ApJ*, 560:821.

Brogan, C. L., Troland, T. H., Roberts, D. A., and Crutcher, R. M. (1999). "DETECTION OF MAGNETIC FIELDS TOWARD M17 THROUGH THE H I ZEEMAN EFFECT". *ApJ*, 513:304.

Brüns, C., Kerp, J., Kalberla, P. M. W., and Mebold, U. (2000). "THE HEAD-TAIL STRUCTURE OF HIGH-VELOCITY CLOUDS. A SURVEY OF THE NORTHERN SKY". *A& A*, 357:120.

Brüns, C. and Mebold, U. (2004). *"High Velocity Clouds"*, volume 312. Springer.

Castelli, F. and Kurucz, R. (2004). "NEW GRIDS OF ATLAS9 MODEL ATMOSPHERES". *astro-ph*, page 0405087.

de Heij, V., Braun, R., and Burton, W. B. (2002). "AN ALL-SKY STUDY OF COMPACT, ISOLATED HIGH-VELOCITY CLOUDS". *A& A*, 392:417.

Duchéne, G., Simon, T., Eislöffel, J., and Bouvier, J. (2001). "VISUAL BINARIES AMONG HIGH-MASS STARS. AN ADAPTIVE OPTICS SURVEY OF OB STARS IN THE NGC 6611 CLUSTER". *A& A*, 379:147.

Ferland, G. (1978). url= http://www.nublado.org/.

Flagey, N., Boulanger, F., Noriega-Crespo, A., Paladini, R., Montmerle, T., Carey, S. J., Gagné, M., and Shenoy, S. (2011). "TRACING THE ENERGETICS AND EVOLUTION OF DUST WITH SPITZER: A CHAPTER IN THE HISTORY OF THE EAGLE NEBULA". *A& A*, 531:A51.

Hall, J. S. and Mikesell, A. H. (1949). "OBSERVATIONS OF POLARIZED LIGHT FROM STARS". *AJ*, 54:187.

Han, J. L., Manchester, R. N., Lyne, A. G., Qiao, G. J., and van Straten, W. (2006). "PULSAR ROTATION MEASURES AND THE LARGE-SCALE STRUCTURE OF THE GALACTIC MAGNETIC FIELD". *ApJ*, 642:868.

Healy, K. R. and Claussen, M. J.and Hester, J. J. (2000). "WATER MASERS AND YSOS IN H II REGIONS: PRELIMINARY RESULTS OF A VLA SURVEY". AAS. 197th AAS Meeting.

Heiles, C. and Troland, T. H. (2004). "THE MILLENNIUM ARECIBO 21 CENTIMETER ABSORPTION-LINE SURVEY. III. TECHNIQUES FOR SPECTRAL POLARIZATION AND RESULTS FOR STOKES V". *ApJS*, 151:271.

Heiles, C. and Troland, T. H. (2005). "THE MILLENNIUM ARECIBO 21 CENTIMETER ABSORPTION-LINE SURVEY. IV. STATISTICS OF MAGNETIC FIELD, COLUMN DENSITY, AND TURBULENCE". *ApJ*, 624:773.

Hester, J. J., Scowen, P. A., Sankrit, R., Lauer, T. R., Ajhar, E. A., Baum, W. A., Code, A., Currie, D. G., Danielson, G. E., Ewald, S. P., Faber, S. M., Grillmair, C. J., Groth, E. J., Holtzman, J. A., Hunter, D. A., Kristian, J., Light, R. M., Lynds, C. R., Monet, D. G., O'Neil, E. J., J., Shaya, E. J., Seidelmann, K. P., and Westphal, J. A. (1996). "HUBBLE SPACE TELESCOPE WFPC2 IMAGING OF M16: PHOTOEVAPORATION AND EMERGING YOUNG SELLAR OBJECTS". *AJ*, 111:2349.

Hill, T., Motte, F., Didelon, P., White, G. J., Marston, A. P., Nguyên Luong, Q., Bontemps, S., André, P., Schneider, N., Hennemann, M., Sauvage, M., Di Francesco, J., Minier, V., Anderson, L. D., Bernard, J. P., Elia, D., Griffin, M. J., Li, J. Z., Peretto, N., Pezzuto, S., Polychroni, D., Roussel, H., Rygl, K. L. J., Schisano, E., Sousbie, T., Testi, L., Thompson, D. W., and Zavagno, A. (2012). "THE M16 MOLECULAR COMPLEX UNDER THE INFLUENCE OF NGC 6611. HERSCHELS PERSPECTIVE OF THE HEATING EFFECT ON THE EAGLE NEBULA". *AA*, 542:A114.

Hiltner, W. A. (1949). "ON THE PRESENCE OF POLARIZATION IN THE CONTINUOUS RADIATION OF STARS. II". *Science*, 109:165.

Kalberla, P. M. W. (2003). "ON THE PRESENCE OF POLARIZATION IN THE CONTINUOUS RADIATION OF STARS. II.". *ApJ*, 588:805.

Kazes, I., Troland, T. H., and Crutcher, R. M. (1991). "ZEEMAN SPLITTING OF H I TOWARD HIGH VELOCITY CLOUDS AND NGC 1275". *A& A*, 245:L17.

Linsky, J. L., Gagn, M., Mytyk, A., McCaughrean, M., and Andersen, M. (2007). "CHANDRA OBSERVATIONS OF THE EAGLE NEBULA. I. EMBEDDED YOUNG STELLAR OBJECTS NEAR THE PILLARS OF CREATION". *ApJ*, 654:347.

Lockman, F. J. (2003). "HIGH-VELOCITY CLOUD COMPLEX H: A SATELLITE OF THE MILKY WAY IN A RETROGRADE ORBIT?". *ApJ*, 591:33.

Lockman, F. J., Benjamin, R. A., Heroux, A. J., and Langston, G. I. (2008). "THE SMITH CLOUD: A HIGH-VELOCITY CLOUD COLLIDING WITH THE MILKY WAY". *ApJ*, 679:21.

Maloney, P. R. and Putman, M. E. (2003). "ARE COMPACT HIGH-VELOCITY CLOUDS EXTRAGALACTIC OBJECTS?". *ApJ*, 589:270.

Mirabel, I. F. and Morras, R. (1990). "CLOUD-MILKY WAY COLLISIONS IN THE OUTER GALAXY". *ApJ*, 356:130.

Oliveira, J. M. (2008). "STAR FORMATION IN THE EAGLE NEBULA". *ASP*, 5:599.

Peek, J. E. G., Putman, M. E.and McKee, C. F., Heiles, C., and Stanimirović, S. (2007). "RECONSTRUCTING DECONSTRUCTION: HIGH-VELOCITY CLOUD DISTANCE THROUGH DISRUPTION MORPHOLOGY". *ApJ*, 656:907.

Pellegrini, E. W., Baldwin, J. A.and Brogan, C. L., Hanson, M. M., Abel, N. P., Ferland, G. J., Nemala, H. B., Shaw, G., and Troland, T. H. (2007). "MAGNETICALLY-SUPPORTED PDR IN M17". *ApJ*, 658:1119.

Preibisch, T., Ossenkopf, V., Yorke, H. W., and Henning, T. (1993). "THE INFLU-ENCE OF ICE-COATED GRAINS ON PROTOSTELLAR SPECTRA". *A&A*, 279:577.

Robishaw, T. and Heiles, C. (2009). "ON MEASURING ACCURATE 21 CM LINE PROFILES WITH THE ROBERT C. BYRD GREEN BANK TELESCOPE". *PASP*, 121:272.

Salama, F. (2008). "PAHs IN ASTRONOMY - A REVIEW". *IAUS*, 251:357.

Sankrit, R. and Hester, J. (2000). "PHOTOIONIZED INTERFACE IN BLISTER H II REGIONS". *ApJ*, 535:847.

Santillan, A., Franco, J., and Kim, J. (2001). "ORIGIN OF THE COMETARY STRUCTURE OF THE HVCS: 3D-MHD NUMERICAL SIMULATIONS". *Journal of the Korean Astronomical Society*, 34:341.

Santillán, A., Franco, J., Martos, M., and Kim, J. (1999). "THE COLLISIONS OF HIGH-VELOCITY CLOUDS WITH A MAGNETIZED GASEOUS GALACTIC DISK". *ApJ*, 515:657.

Schuller, F., Leurini, S., Hieret, C., Menten, K. M., Philipp, S. D., Gsten, R., Schilke, P., and Nyman, L.-Å. (2006). "MOLECULAR EXCITATION IN THE EAGLE NEBULAS FINGERS". *AA*, 454:87.

Tielens, A. (2008). "INTERSTELLAR POLYCYCLIC AROMATIC HYDRO-CABON MOLECULES". *ARAA*, 46:289.

Tielens, A. G. G. M. and Hollenbach, D. (1985). "PHOTODISSOCIATION RE-GIONS. I. BASIC MODEL". *ApJ*, 291:722.

Verschuur, G. L. (1969). "MEASUREMENTS OF MAGNETIC FIELDS IN INTER-STELLAR CLOUDS OF NEUTRAL HYDROGEN". *ApJ*, 156:861.

Wakker, B. P. and van Woerden, H. (1997). "HIGH-VELOCITY CLOUDS". *ARA&A*, 35:217.

Ward-Thompson, D., Kirk, J. M., André, P., Saraceno, P., Didelon, P., Könyves, V., Schneider, N., Abergel, A., Baluteau, J.-P., Bernard, J.-P., Bontemps, S., Cambrésy, L., Cox, P., di Francesco, J., di Giorgio, A. M., Griffin, M., Hargrave, P., Huang, M., Li, J. Z., Martin, P., Men'shchikov, A., Minier, V., Molinari, S., Motte, F., Olofsson, G., Pezzuto, S., Russeil, D., Sauvage, M., Sibthorpe, B., Spinoglio, L., Testi, L., White, G., Wilson, C., Woodcraft, A., and Zavagno, A. (2010). "A HERSCHEL STUDY OF THE PROPERTIES OF STARLESS CORES IN THE POLARIS FLARE DARK CLOUD REGION USING PACS AND SPIRE". *A&A*, 518:92.

Westmeier, T. (2007). *"THE RELICS OF STRUCTURE FORMATION: HIGH-VELOCITY CLOUDS AROUND THE ANDROMEDA GALAXY AND THE MILKY WAY"*. PhD thesis, Rheinischen Friedrich-Wilhelms-Universisät Bonn.

White, G. J., Nelson, R. P., Holland, W. S., Robson, E. I., Greaves, J. S. an McCaughrean, M. J., Pilbratt, G. L., Balser, D. S., Oka, T. andd Sakamoto, S., Hasegawa, T., McCutcheon, W. H., Matthews, H. E., Fridlund, C. V. M., Tothill, N. F. H., Huldtgren, M., and Deane, J. R. (1999). "THE EAGLE NEBULAS FINGERS POINTERS TO THE EARLIEST STAGES OF STAR FORMATION?". *AA*, 342:233.

Vita

Furea Kiuchi

- **Date and place of birth:**

  – March 22, 1985 Chiba Japan

- **Educational institutions attended and degrees awarded:**

  – M.S. in Physics & Astronomy, University of Kentucky, 2010

  – B.S. in Physics & Astronomy, University of Washington, 2007

- **Professional position held:**

  – Teaching Assistant, University of Kentucky, 2007-2012

- **Professional publications**

  – *"The Milky Way Tomography with SDSS. III. Stellar Kinematics"* Bond, Nicholas A.; Ivezič, Željko; Sesar, Branimir; Jurič, Mario; Munn, Jeffrey A.; Kowalski, Adam; Loebman, Sarah; Rokar, Rok; Beers, Timothy C.; Dalcanton, Julianne; Rockosi, Constance M.; Yanny, Brian; Newberg, Heidi J.; Allende Prieto, Carlos; Wilhelm, Ron; Lee, Young Sun; Sivarani, Thirupathi; Majewski, Steven R.; Norris, John E.; Bailer-Jones, Coryn A. L.; Re Fiorentin, Paola; Schlegel, David; Uomoto, Alan; Lupton, Robert H.; Knapp, Gillian R.; Gunn, James E.; Covey, Kevin R.; Allyn Smith, J.; Miknaitis, Gajus; Doi, Mamoru; Tanaka, Masayuki; Fukugita, Masataka; Kent, Steve; Finkbeiner, Douglas; Quinn, Tom R.; Hawley, Suzanne; Anderson, Scott; **Kiuchi, Furea**; Chen, Alex; Bushong, James; Sohi, Harkirat; Haggard, Daryl; Kimball, Amy; McGurk, Rosalie; Barentine, John; Brewington, Howard; Harvanek, Mike; Kleinman, Scott; Krzesinski, Jurek; Long, Dan; Nitta, Atsuko; Snedden, Stephanie; Lee, Brian; Pier, Jeffrey R.; Harris, Hugh; Brinkmann, Jonathan; Schneider, Donald P., 2010, ApJ, 716, 1

  – *"The Milky Way Tomography with SDSS. II. Stellar Metallicity"* Ivezič, Željko, Sesar, Branimir; Juri, Mario; Bond, Nicholas; Dalcanton, Julianne; Rockosi, Constance M.; Yanny, Brian; Newberg, Heidi J.; Beers, Timothy C.; Allende Prieto, Carlos; Wilhelm, Ron; Lee, Young Sun; Sivarani, Thirupathi; Norris, John E.; Bailer-Jones, Coryn A. L.; Re Fiorentin, Paola; Schlegel, David; Uomoto, Alan; Lupton, Robert H.; Knapp, Gillian R.; Gunn, James E.; Covey, Kevin R.; Smith, J. Allyn; Miknaitis, Gajus; Doi, Mamoru; Tanaka, Masayuki; Fukugita, Masataka; Kent, Steve; Finkb-

einer, Douglas; Munn, Jeffrey A.; Pier, Jeffrey R.; Quinn, Tom; Hawley, Suzanne; Anderson, Scott; **Kiuchi, Furea**; Chen, Alex; Bushong, James; Sohi, Harkirat; Haggard, Daryl; Kimball, Amy; Barentine, John; Brewington, Howard; Harvanek, Mike; Kleinman, Scott; Krzesinski, Jurek; Long, Dan; Nitta, Atsuko; Snedden, Stephanie; Lee, Brian; Harris, Hugh; Brinkmann, Jonathan; Schneider, Donald P.; York, Donald G., 2008, ApJ, 684, 287